Thorium isotopes in the Southeast Atlantic Ocean: Tracking scavenging during water mass mixing along neutral density surfaces

Matthieu Roy-Barman, François Thil, Louise Bordier, Arnaud Dapoigny, Lorna Foliot, Sophie Ayrault, François Lacan, Catherine Jeandel, Catherine Pradoux, Ester Garcia-Solsona

Thorium isotopes in the Southeast Atlantic Ocean: Tracking scavenging during water mass mixing along neutral density surfaces

Matthieu Roy-Barman[1], François Thil[1], Louise Bordier[1], Arnaud Dapoigny[1], Lorna Foliot[1], Sophie Ayrault[1], François Lacan[2], Catherine Jeandel[2], Catherine Pradoux[2], Ester Garcia-Solsona[2,3]

[1] Laboratoire des Sciences du Climat et de l'Environnement, LSCE-IPSL (CEA CNRS UVSQ), Université Paris-Saclay, Orme des Merisiers - centre de Saclay, 91191 Gif-sur-Yvette, France

[2] LEGOS (CNRS/CNES/IRD/Université de Toulouse), Observatoire Midi-Pyrénées, 31400 Toulouse, France

[3] Dinàmica de la Terra i de l'Oceà, Facultat de Ciències de la Terra, Universitat de Barcelona, 08028 Barcelona, Spain.

Submitted to Deep Sea Research

Revised version

Version 2.0

May 1st 2019

Abstract

The distributions of dissolved and particulate thorium isotopes (^{230}Th and ^{232}Th) were established in samples from the BONUS GoodHope (BGH) IPY-GEOTRACES cruise in the SE Atlantic sector of the Southern Ocean (36°S-13°E to 57°S-0°, Feb.–Mar. 2008). The distribution of total (dissolved+particulate) ^{232}Th is dominated by the inputs from continental margins. The non-linear profiles of dissolved ^{230}Th are interpreted as due to the southward upwelling of the isopycnal surfaces. However, total ^{230}Th and ^{232}Th versus salinity plots illustrate departures from binary mixing and provides evidence for non-conservative behavior of both isotopes along the section. We propose a model for total ^{230}Th and ^{232}Th scavenging and mixing along isopycnal surfaces. We use this model to estimate particle settling speeds and isopycnal eddy diffusion coefficients along the BGH section. Data-model comparison suggests particle settling velocities in the range of 400-700 m/y and isopycnal eddy diffusivity of the order of 2000 m^2/s.

Keywords: thorium isotopes, Southern Ocean, Atlantic, marine particles, isopycnal mixing

Highlights:

Small deviations of thorium isotopes from a conservative behavior occurs during isopycnal mixing through the ACC.

An advection-diffusion-scavenging model along neutral density surface is applied to thorium isotopes.

Combining thorium isotopes allows constraining particle settling speeds and isopycnal mixing coefficients

65
66
67
68
69
70

1. Introduction

Thorium isotopes are recognized tracers of particle dynamics in the ocean that provide key information on ocean biogeochemical cycles (Bacon and Anderson, 1982, Nozaki et al., 1981, Roy-Barman et al., 1996). In particular, ^{230}Th is produced *in situ* by radioactive decay of ^{234}U and rapidly scavenged on marine particles, thus providing a chronometer for estimating the settling speed for marine particles. ^{232}Th is introduced in the ocean by continental inputs and hence can bring complementary information on marine particles compared to ^{230}Th (Roy-Barman et al., 2002).

In early studies, particle settling speeds were derived from ^{230}Th with a simple 1D (vertical) production-scavenging model, which was well adapted to oceanic areas with weak currents (Bacon and Anderson, 1982, Nozaki et al., 1981, Roy-Barman et al., 1996, Roy-Barman, 2009). However, it is now clear that strong currents characterizing oceanic regions such as the Southern Ocean may significantly affect the distribution of ^{230}Th in the water column and hence potentially bias the estimate of the settling speed of marine particles obtained by the simple production-scavenging model. Therefore, a simple production-scavenging-advection model was proposed to constrain simultaneously the renewal rate of the deep waters and the settling speed of marine particles in the Atlantic sector of the Southern Ocean (Rutgers van der Loeff et al., 1996). However, it relies on rather crude approximations, such as uniform values for ventilation rate and particle settling speed over the whole water column. Another limitation of this model is that it does not consider the mixing of water masses with different origins and Th contents.

In the real ocean, the distribution of geochemical tracers depends on both non-conservative processes and mixing of water masses of different origins, in addition to advection by currents. This mixing is thought to occur preferentially along surfaces of constant density called isopycnal surfaces. Chase et al. (2003) suggested that the small gradients in ^{230}Th concentration observed along neutral density surfaces in the deep waters of the Southern Ocean argue for small eddy diffusive fluxes and little scavenging of ^{230}Th across the Antarctic Polar Front (APF). However, they also advocated for further work to better constrain both nuclide concentrations along isopycnal surfaces and diffusion coefficients in the Southern Ocean.

In the present work, we take advantage of high precision ^{230}Th data collected during the Bonus GoodHope cruise to revisit the behavior of ^{230}Th across the Southern Ocean and to try to unravel the respective roles of water mass mixing and particle scavenging along neutral

density surfaces. Our goal is to explore if Th data can help constraining both particle settling speeds and water mixing rates using a model that is more complete than with the simple mixing-scavenging model.

2. Sampling and methods

2.1. Hydrographic settings

The oceanographic structure determined from the Bonus GoodHope (BGH) expedition has already been described (Chever et al., 2010, Bown et al., 2011, Garcia-Solsona et al., 2014, Abadie et al., 2017), so we only summarize the main features and focus on the 5 super stations (S1–S5 stations, Fig. 1) sampled for Th isotopes. Three main hydrological and circulation regimes characterize the studied area: the Subtropical domain (Station S1), the Antarctic Circumpolar Current (ACC; S2 to S4) and the Weddell Sea Gyre (S5). The subtropical domain is bounded to the south by the subtropical front (STF), which was located around 41°S-42°S, north of S2. The ACC domain, incorporating the Subantarctic Front (SAF; ~45°S) and the Polar Front (PF; ~50°S), is bounded to the south by the southern ACC boundary (Sby). From the Sby to the Antarctic continent, water circulation is dominated by the cyclonic Weddell Gyre (WG; S5).

The subtropical regime is influenced from 0 down to ~800 m by surface and intermediate waters of Indian Ocean origin ($\theta \geq 10$ °C, $S \geq 34.5$), conveyed south of Africa by the Agulhas Current and detached eddies (Gladyshev et al., 2008). At intermediate depths (~300–900 m), Antarctic Intermediate Water (AAIW) originates from cooled surface waters of the ACC that are subsequently subducted northward at the PF. Two varieties of AAIW have been recognized from BGH cruise data: one originating from the Indian Ocean (i-AAIW) close to the African continent ($S > 34.3$; S1) and one formed in the Atlantic Ocean (a-AAIW; $S < 34.3$; S2–S4). The Upper Circumpolar Deep Water (UCDW; ranging from 500 to 2000 m depth) is identified below the AAIW and upwells southwards. Below UCDW, the eastward flowing (and southward drifting) NADW is detected by its salinity maximum within the 2000–3000 m depth range. Two NADW branches are identified in the BONUS section: North of the Agulhas Ridge, higher salinities indicate advection by an eastern boundary current referred to as SE-

NADW (S1 and S2 stations). South of the Agulhas Ridge, the main (western) component of NADW (i.e., SW- NADW; S2-S4 stations) is incorporated into the ACC after flowing southward along the Argentine-Brazilian margin (Stramma and England, 1999). The other water mass encountered at southern ACC latitudes is high salinity Lower Circumpolar Deep Water (LCDW). Cold and fresher Antarctic Bottom Water (AABW) is also recognized, occupying the water column from LCDW/NADW depths down to the sea floor (Fig. 2). In the Weddell Sea Gyre domain (S5), we interpret deep oxygenated waters as due to input of recently ventilated AABW.

Water mass transport along the BGH section is mainly zonal. In the subtropical domain (station S1), it is dominated by the westward flowing Agulhas Current in the upper water column ($z < 1500$ m) and at depth by the eastward transport of SE-NADW as delineated by Sokolov and Rintoul (2009). Stations S2, S3 and S4 are located within the Antarctic Circumpolar Current, flowing eastward throughout the water column. Finally station S5 is located in the Northern limb of the Weddell gyre, also flowing eastward. Therefore, the BGH section is approximately perpendicular to the climatological mean (dominant) flows, so that water masses should not flow directly from one BGH station to another. The different BGH stations would therefore not be directly connected by the mean flow. However, superimposed on this vigorous zonal circulation, slower meridional transports are clearly visible on meridional sections of water mass tracers such as salinity, temperature or nutrients, revealing notably the northward transport of AAIW and AABW, and southward transport of NADW (Abadie et al., 2017). This meridional transport is presumably a residual circulation in which lateral eddy fluxes largely balance the wind-driven circulation (Marshall and Speer, 2016). While the circulation in the BGH area is therefore clearly 3D and dominated by zonal flows (preventing a direct link by mean advection between our 5 stations), some of the BGH samples can still reflect the effect of these meridional transports of these water masses upstream of the BGH section. In the following, transport models will be used to link tracer properties measured along the BGH section. We do not assume that the transports actually act along the BGH section (pure meridional transport is not realistic). However, we use the tracer properties measured along the BGH section to elucidate and quantify the meridional component (advection, diffusion) embedded within a dominant zonal component and therefore acts upstream of the BGH section, for instance between the Drake Passage and the BGH section.

2.2. Sampling

The BONUS GoodHope cruise took place in the framework of the international polar year (IPY) from February 8th 2008 till March 17th 2008 on board the Research Vessel Marion-Dufresne II, from 34°S 18°E to 51°S 00°W and from 51°S to 58°S along the Greenwich meridian. The expedition took place during the late austral summer, when biological activity is high and ice cover is reduced. Five depth profiles (S1–S5 stations) were sampled for both dissolved and particulate Th with 10 or 11 depths per profile with 1 duplicated sample at stations S3, S4 and S5 (Fig. 1). An intercalibration (hereafter referred to as 'intercal') station was analyzed for 3 depths which were all duplicated.

Seawater samples were collected using Niskin bottles equipped with Teflon coated strings and mounted on a rosette frame with a CTD sensor. Challenger Oceanic *in situ* pumps (ISP) were used to filter large seawater volumes through SUPOR filters (pore size: 0.45 µm, filter diameter: 293 mm). Typically, volumes ranging from 200 L to 1000 L were filtered.

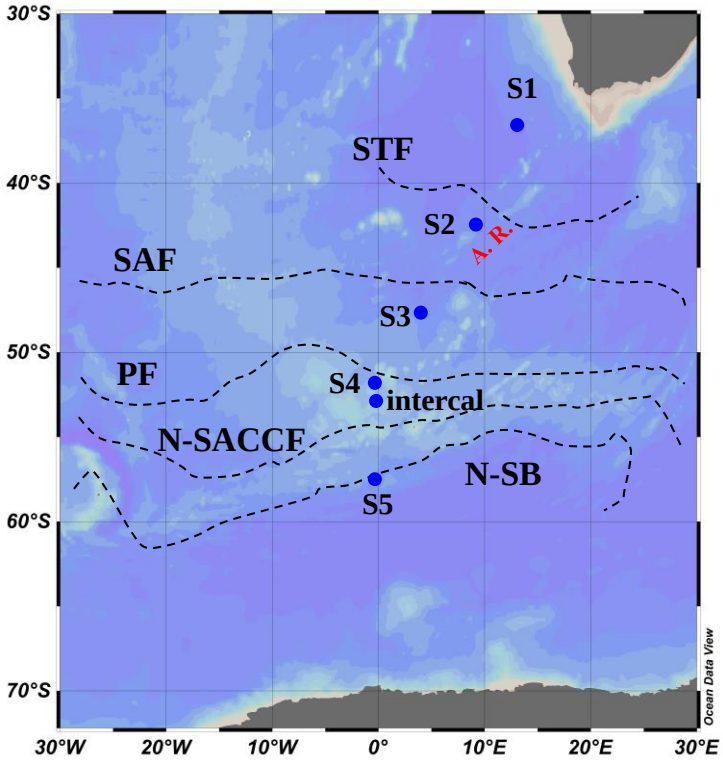

Fig. 1. Sampling stations during the BONUS-GoodHope section and main fronts (following Sokolov and Rintoul, 2009; mean path position): STF = SubTropical Front; SAF = SubAntarctic Front (middle branch); PF = Polar Front (middle branch); N-SACCF = northern branch of the Southern ACC front; N-SB = northern branch of the Southern Boundary. A.R.: Aghulas Ridge.

1849388096 1849388096

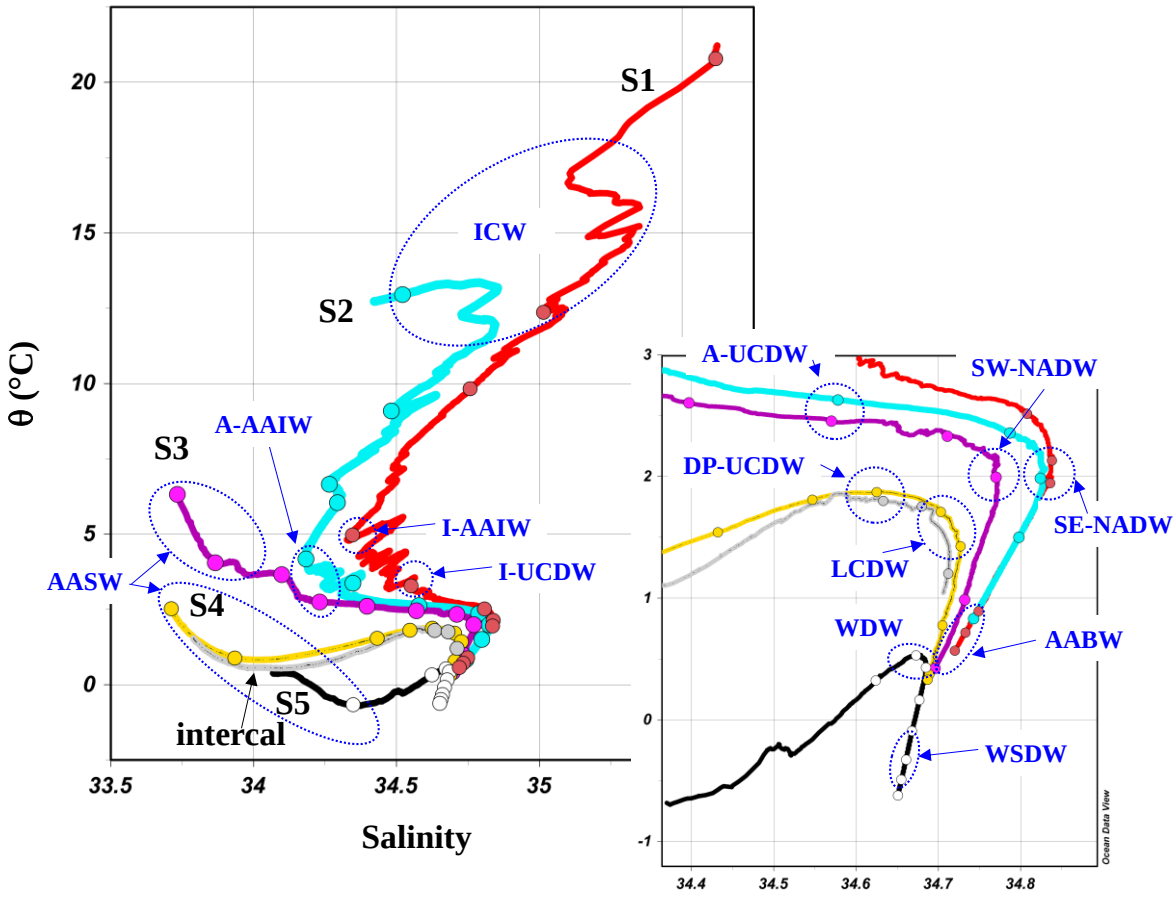

Fig.2: Potential temperature-salinity data during BGH. (a): full depth profiles. (b): deep waters. Dots: data at the depth of dissolved Th samples. Acronyms: AABW, Antarctic Bottom Water; AASW, Antarctic Surface Water; I-AAIW and A-AAIW, Antarctic Intermediate Water of Indian and Atlantic origins; I-CW, Indian Central Water; I-UCDW, A-UCDW, and DPUCDW, Indian, Atlantic, and Drake Passage Upper Circumpolar Deep Water; LCDW, Lower Circumpolar Deep Water; SE-NADW and SW-NADW, Southeast and Southwest North Atlantic Deep Water; WDW, Warm Deep Water; WSDW, Weddell Sea Bottom Water; WW, Winter Water.

2.3. Analytical procedure

Filtered seawater

Twenty liters of filtered seawater (Nuclepore, 90 mm diameter, 0.4 µm pore size) were acidified, spiked with ^{229}Th and pre-concentrated on board using the ferric hydroxide co-precipitation technique as described in Piepgras et al. (1979). The precipitate was then recovered on filters (Supor, 90 mm, 0.4 µm), which were kept in petri dishes and stored in the dark. Back in the laboratory, the filters were submerged in 40 mL of 6 M HCl for 24 h in 300 mL Polytetrafluoroethylene beakers, enabling the dissolution of precipitate. The filters were then carefully rinsed with deionized water to recover all the dissolved precipitate. After

evaporation, the residue was dissolved in 0.5 mL 7M HNO_3 and loaded on an anion-exchange column (AG1-X8 resin, 200–400 mesh) to separate the thorium fraction from the major elements, uranium and the rare earth elements (REE) (adapted from Jeandel et al., 2011). The total ^{232}Th chemical blank is typically 48 ± 14 pg and represents generally less than 15% of the sample although peaks with 50% of the sample occur for very ^{232}Th-poor samples. Total ^{230}Th chemical blank is typically 2.3 ± 0.1 fg and represents generally less than 5 % of the sample although peaks with 30% of the sample occur for very shallow samples.

Particles collected from Niskin bottle filtrations

From the twenty liter seawater samples used for dissolved Th analyses (described above), particulate samples were also available on the 90mm diameter 0.4µm porosity Nuclepore membranes used for filtration (hereafter referred to as Niskin filtration). Membranes were transferred from their petri dishes to Teflon beaker containing 15mL 6M HCl and 2.5mL 15M HNO_3. They were heated 90 minutes at 130°C. After leaving them cool, 0.5mL 23M HF was added, and the mixture was heated again as previously. The membranes were removed from the leaching solutions and rinsed over the beakers with milliQ water. After evaporation, the samples were dissolved in 3mL 0.32M HNO_3 for analysis by Quadrupole Induced Coupled Plasma Mass Spectrometry.

Particles collected from in situ pump filtrations

Filters from the in situ pumps were cut into pieces using ceramic scissors. Several leaching steps were necessary to recover Th without attacking the filters. Filter pieces were first leached with 200 mL of 6N HCl and 1.5 mL of 24-25N HF in a 300 mL Teflon beaker for 2 days at 75°C. The filter pieces were removed from the leaching solution and rinsed with a MQ water squeeze bottle over the leaching beaker. The filter pieces were saved apart. The leaching and rinsing solutions were evaporated down to ~10 mL and transferred into a 30 mL Teflon beaker. Then, the filter pieces were leached a second time with 150 mL of 7N HNO_3 and 0.05 mL of 29N HF for 2 days at 75°C. The filter pieces were removed from the leaching solution and rinsed with MQ water that was again recovered into the leaching beaker. After evaporation to a few mL, this solution was added to the first leaching/rinsing solution. The 300 mL Teflon beaker was rinsed in warm diluted HNO_3 to remove any particle sticking on the beaker walls and the resulting solution was also added to the 30 mL beaker. The resulting solution was then

spiked with ^{229}Th (and ^{233}Pa), dried and dissolved again in a solution with 4 mL of 14N $HNO_3$and 1 mL of 12N HCl. After 1 night on a hot plate, the solution was dried and the residue was dissolved again in 10 ml of 1N HNO_3. Since filters were not rinsed immediately after filtration with distilled water on board, it was preferable to remove the salt before the column chemistry. Therefore, 40µL of a Fe solution (60 mg/g) were added. After 1h-heating, Fe was precipitated by raising the pH to about 8 with NH_3. The Fe precipitate (that coprecipitates Th isotopes) was separated by centrifugation and rinsed several times. Finally, it was dissolved in 0.25 ml of 8N HNO_3, ready for loading on an anionic column. Th isotopes were separated from Fe by ion exchange chromatography on a small volume (0.5 ml) column of AG1X8 resin (200-400 mesh) with a procedure adapted from Jeandel et al., 2011 (Gdaniec et al., 2018).

The total ^{232}Th chemical blank was typically 42 ± 25 pg, although few blanks as high as 1400 pg were observed. Given the good agreement between the particulate ^{232}Th concentrations obtained with the Niskin filtrations (see Fig. ES1) and the ISP ^{232}Th concentrations corrected with the low blank values, the highest blanks were not taken into account to correct the ISP data. Total ^{230}Th chemical blank was typically 1 ± 1 fg. As for ^{232}Th, a small number of very large blanks (up to 125 fg) were obtained but assumed to be outliers.

Mass spectrometry

For dissolved and in situ pump samples, Th isotopes were measured on a MC-ICPMS Neptune + (Thermo-Fischer). The dissolved samples were analyzed with the initial configuration of the Neptune + with an Apex desolvator. The particulate samples were analyzed after the Neptune's upgrade with a Jet interface and an Aridus 2 desolvating nebulizer. The acquisition conditions are given in Gdaniec et al. (2018). The accuracy of the MC-ICPMS measurement was checked by analysis of Th standard IRMM035 (^{230}Th/^{232}Th = $(11.31\pm0.12)\times10^{-6}$, n=6) and IRMM036 $(3.059\pm0.033)\times10^{-6}$, n=8), in good agreement with reference values: ^{230}Th/^{232}Th = $(11.38\pm0.10)\times10^{-6}$ for IRMM035 and ^{230}Th/^{232}Th = $(3.047\pm0.024)\times10^{-6}$ for IRMM036 (Sims et al., 2008). The quality of the analyses was checked through the GEOTRACES intercalibration exercise where we obtained precise and accurate dissolved Th concentrations well within the consensus values (Anderson et al., 2012).

For Niskin filtration samples, ^{232}Th was analyzed by quadrupolar ICPMS (Agilent 7500CE of the Observatoire Midi Pyrénées, Toulouse). Indium and rhenium (100 ppt, added to the samples) were used as internal standards to monitor instrument sensitivity variations.

Reproducibility calculated from 3 duplicated samples (2 different Niskins) was on average 12% (2 standard deviations). Detection limit was 0.5 pg/kg.

3. Results

3.1. Dissolved thorium

Dissolved ^{232}Th concentrations ($^{232}Th_d$) range from 4.7 pg/kg to 288 pg/kg (Fig. 2a, Tab. ES 1) and generally increase with depth. At stations S1 and S2, the $^{232}Th_d$ profiles have a local maximum around 200-400 m depth and a sharp increase at bottom depths. Conversely, at station S3, $^{232}Th_d$ for the deepest sample is relatively low. This feature was also noted for dissolved REE (Garcia-Solsona et al. 2014) and for $^{230}Th_d$ (see below) analyzed on the same water sample. Along the section, the lowest $^{232}Th_d$ are found at station S3 and S4, far from the coasts of Africa and Antarctica ($^{232}Th_d$ = 4.7-30 pg/kg). All the $^{232}Th_d$ duplicates agree within analytical uncertainties.

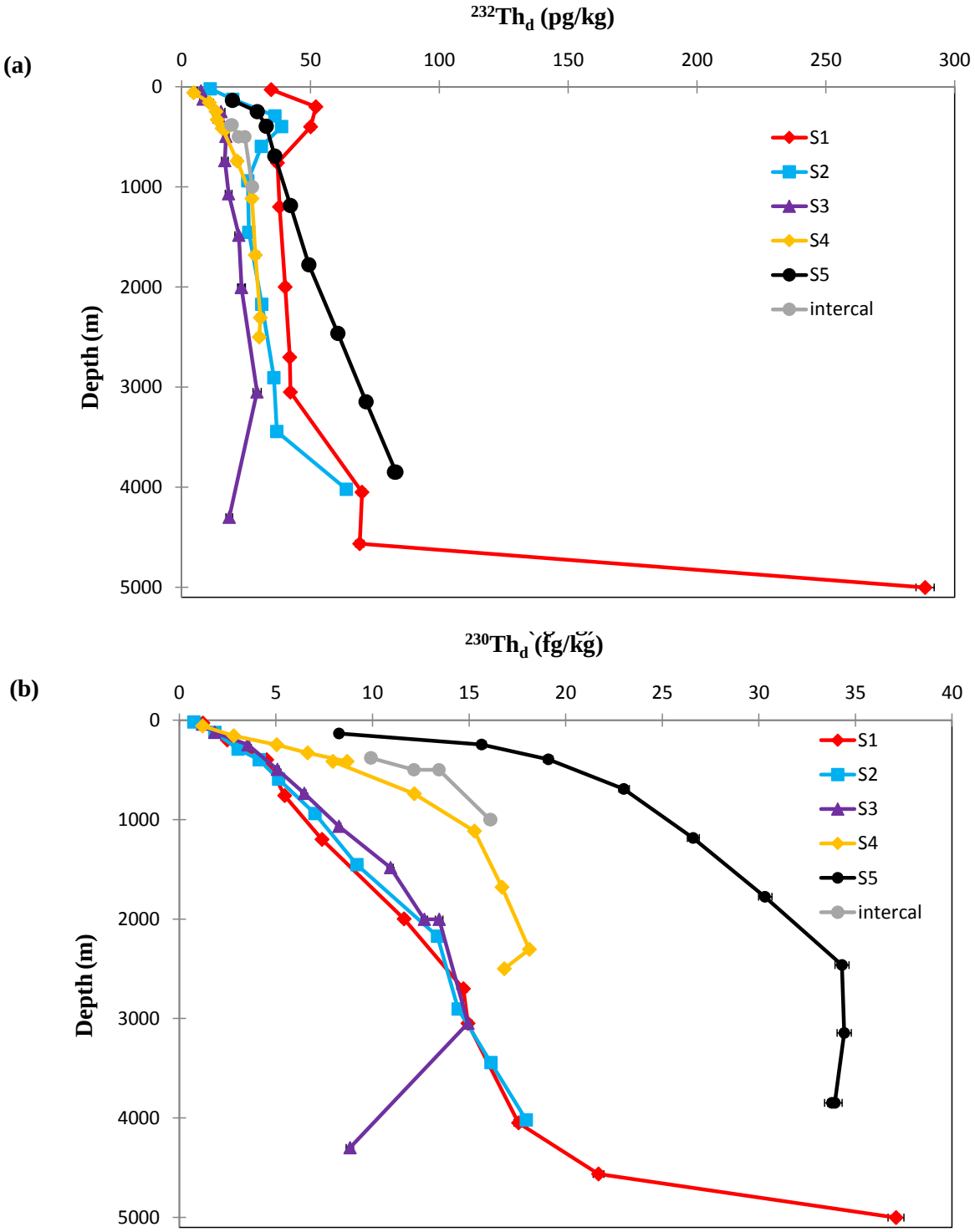

Fig. 3. Dissolved thorium profiles. a: dissolved ^{232}Th. b: dissolved ^{230}Th.

Dissolved ^{230}Th concentrations ($^{230}Th_d$) range from 0.7 fg/kg to 37 fg/kg (Fig. 3b) and generally increase with depth. At stations S1 and S2, the $^{230}Th_d$ profiles increase approximately linearly from the surface down to 4000 m depth. At station S1, there is a sharp increase of $^{230}Th_d$ above the seafloor. Conversely, at station S3, S4 and S5, the $^{230}Th_d$ profiles have concave shapes and, for a given depth, $^{230}Th_d$ is higher at stations S4 and S5 than at S1, S2 and S3. All $^{230}Th_d$ duplicates agree within 9% (3 of them agreeing within the analytical uncertainties).

Following GEOTRACES good practices, a comparison with 2 stations of the Zero-Drake cruise (Rutgers van de Loeff et al., 2016) is provided (Fig. ES3). Profiles agree within uncertainties for ^{230}Th and more qualitatively for ^{232}Th.

3.2. Particulate thorium

Particulate ^{232}Th concentrations ($^{232}Th_p$) have been already reported elsewhere (Garcia-Solsona et al., 2014). $^{232}Th_p$ from ISP filtrations range from 0.08 pg/kg to 371 pg/kg (Fig. 4a, Tab. ES2). There is generally a good agreement between $^{232}Th_p$ profiles obtained with in situ pumps and profiles obtained with Niskin filtrations. The most notable exception is above the seafloor at station S3, where Niskin bottle filtration gives $^{232}Th_p$ = 27 pg/kg, whereas ISP filtration gives $^{232}Th_p$ = 2.5 pg/kg. Apart from this particular feature recorded at S3, the $^{232}Th_p$ profiles generally increase with depth with a sharp increase above the seafloor. Along the section, the highest $^{232}Th_p$ concentrations are found at station S1 and S2, which are the stations closest to the African coast.

All the $^{232}Th_p$ duplicates agree within analytical uncertainties. The variation in $^{232}Th_p$ observed between in situ pumps and Niskin filtrations (Fig. ES1) is of the same order than observed for other insoluble elements (Planquette and Sherrell, 2012).

Particulate ^{230}Th concentrations ($^{230}Th_p$) range from 0.02 fg/kg to 28 fg/kg (Fig. 4b). $^{230}Th_p$ generally increase with depth. At stations S1 and S2, the $^{230}Th_p$ profiles increase approximately linearly from the surface down to 4000 m depth and then present a sharp increase of $^{230}Th_p$ above the seafloor (height above the seafloor is 295 m and 212 m at, respectively, S1 and S2). At station S3, $^{230}Th_p$ decreases just above the seafloor similarly to $^{232}Th_d$ (height above the seafloor is 218 m at S3).

Two in situ pump filtrations were replicated. At station S3 and 3050-m depth, the replicates agree within 4% for both $^{232}Th_p$ and $^{230}Th_p$. At station S4 and 1130-m depth, both the $^{232}Th_p$ and $^{230}Th_p$ concentrations differ by a factor of ~2, suggesting either a problem of volume measurement, data recording or a loss of particles during the filter handling. We choose to use the concentrations measured on the filter with the largest filtered volume of water, because it corresponds to the $^{232}Th_p$ concentration closest to the Niskin filtration.

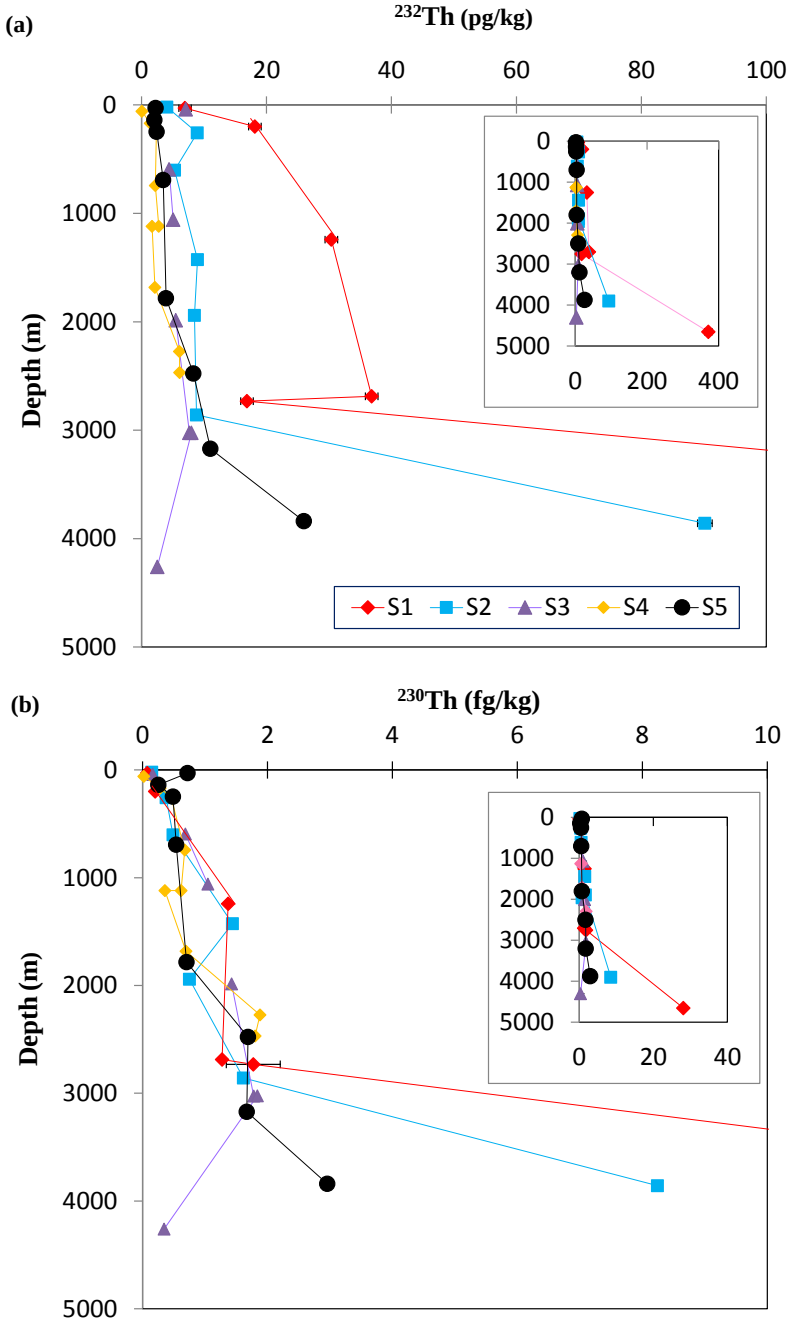

Fig. 4. Particulate Thorium profiles collected with *in situ* pumps. (a) Particulate ^{232}Th. (b) Particulate ^{230}Th. Insets: expanded concentration scales to display particulate concentration maximum at S1.

4. Discussion

4.1. ^{230}Th profiles

The dissolved ^{230}Th profiles obtained during Bonus GoodHope are consistent with previous results from the South Atlantic and the Weddell Sea (Rutgers van der Loeff and Berger, 1993, Rutgers van der Loeff et al., 2016). Station S1 has a relatively linear profile from the surface down to 3000 m deep. This is consistent with the 1D reversible scavenging model, in which ^{230}Th is only transported vertically by reversible scavenging on settling particles. However, even though S1 is located in the subtropical gyre, north of the subtropical front, the profile is not perfectly linear. This presumably reflects the influence of surface and intermediate waters advected from the Indian Ocean (ICW and AAIW down to ~1200 m) and deep water advected from the Atlantic Ocean (SE-NADW). The ^{230}Th content of the surface and intermediate waters at S1 compare well with those reported in the south Indian Ocean (^{230}Th ≈ 4-5 fg/kg at 500 m, Thomas et al., 2006). The ^{230}Th contents of deep waters (^{230}Th ≈ 13 fg/kg at 2000 m) at S1 are on the low side of those reported for SE-NADW sampled off Namibia (^{230}Th ≈ 12-24 fg/kg at 2000 m, Scholten et al. 2008) and that flows towards S1 (Arhan et al., 2003), suggesting the imprint of boundary scavenging. The deepest parts of the S1 profile significantly deviate from the linear increase: the higher dissolved and particulate ^{230}Th (as well as ^{232}Th) concentrations suggest a release from the South African margin sediments.

From the surface down to 3000 m depth, the ^{230}Th profiles of S2 and S3 are similar to S1. In the deepest waters, S2 has a strong increase of its dissolved and particulate ^{230}Th (although less than S1) also suggesting inputs from the sediments or lateral transport from the African margin. By contrast, at S3, the low ^{230}Th$_d$ concentrations at a depth of 4500 m could also be attributed to bottom scavenging (a low REE content on the same sample was also noted by Garcia-Solsona et al., 2014).

The strongly concave shapes of the ^{230}Th$_d$ profiles at S4 and S5 strongly suggests these profiles are impacted by the upwelling of LCDW (Rutgers van der Loeff and Berger, 1993). The ^{230}Th$_d$ profile at S3 has also a concave shape that can be regarded as a result of the LCDW upwelling. However, above 3000 m depth, it is not so different from the S1 profile where no

LCDW upwelling is suspected. Also, the low $^{230}Th_d$ concentrations at a depth of 4500 m, that accentuate the nonlinearity of the profile, could also be attributed to bottom scavenging.

At stations S1, S2 and S3, the $^{230}Th_p$ profiles have very similar slopes, particularly from the surface down to 1500 m depth. We consider the conservation equation of the 1D reversible scavenging model at steady state (and neglecting ^{230}Th radioactive decay):

$$\frac{\partial C_t}{\partial t} = P_d - w_p \frac{\partial C_p}{\partial z} = 0 \qquad (2)$$

Where C_t is the total (dissolved + particulate) ^{230}Th concentration, P_d is the in situ production rate of ^{230}Th (P_d = 0.56 fg/kg/y), w_p is the particle settling speed and C_p the particulate ^{230}Th concentration. Hence, w_p is given by: $w_p = P/(\partial^{230}Th_p/\partial z)$. Using an average slope of 0.001 fg/kg/m, we obtain that w_p = 560 m/d, in agreement with Rutgers van der Loeff and Berger (1993).

In the southern part of the section, we first use the mixing-scavenging model introduced by Rutgers van der Loeff and Berger (1993) to evaluate the impact of lower Circumpolar Deep Water upwelling and input into the Weddell Gyre. This "scavenging-mixing" model relies on several assumptions:

(i) The representation of mixing with a constant restoring term at all depths (eq. 3). This is largely ad hoc, so that the physical interpretation of C_{it} and τ_w is unclear.

(ii) the omission of the effects of vertical transport by advection and diffusion,

(iii) steady state,

(iv) the partition coefficient K is vertically uniform. It implies that the $^{230}Th_{xs}$ particulate fraction is constant over the depth profile. Clear variations of the $^{230}Th_{xs}$ particulate fraction (Tab. ES2) occur in the deepest samples either due to particle inputs from the margins (stations S1, S2 and S5, see Gdaniec et al., 2019) or following hydrothermal scavenging (station S3).

(v) K is very small compared to 1, so that C_d could be approximated by C_t. Apart for the deepest samples at stations S1 and S2, it introduces an underestimation of w_p by 13 % at most.

(vi) the particle settling velocity w_p is vertically uniform. This assumption is deduced the from linear dissolved and particulate ^{230}Th profiles observed in regions unaffected by strong deep currents (Roy-Barman et al., 1996).

(vii) C_d is negligible near the surface.

Using the above assumptions, the tracer conservation equation of this model is:

$$\frac{\partial C_t}{\partial t} = P_d + \frac{(C_{i\_t} - C_t)}{\tau_w} - w_p \frac{\partial C_p}{\partial z} = 0 \qquad (3)$$

Where τ_w is restoring time scale taken equivalent to the water residence time and C_{i_t} is the total ^{230}Th concentration of the inflowing water. Introducing a partition coefficient between dissolved and particulate Th, $K = C_p / C_d$ and integrating equation 3 vertically over the water column, the $^{230}Th_d$ concentration at any depth is given by:

$$C_d = \left(C_{i\_t} + P_d \tau_w\right) \times \left(1 - \exp\left(-\frac{z}{w_p K \tau_s}\right)\right) \qquad (4)$$

For station 5, we use the $^{230}Th_i$ = 24 fg/kg for the LCDW (Rutgers van der Loeff and Berger, 1993), K=0.04 is the average ratio measured at this station. Then, we adjust w_p = 875 m/y and τ_w= 20 y to obtain a good agreement between the modelled curve and the data (Fig. 5). The low τ_w obtained here compared to 45 y used by Rutgers van der Loeff and Berger (1993) derives presumably from the relatively peripheral position of station S5 in the Weddell Sea. We confirm that the scavenging residence time in the Weddell Sea (τ_s=d/(2Kw_p) = 55 y for a water column of a depth of d = 4000 m) is larger than in the subtropical gyre (τ_w = 25 y for a water column of a depth of 4000 m). On the whole, the model explains why the $^{230}Th_d$ concentrations are high and do not increase linearly with depth in the Weddell Gyre.

We apply the same model to station S4. Here $^{230}Th_i$ is also adjusted to obtain a good data-model agreement. We note that 2 modeled curves based on relatively different sets of τ_w and w_p values (ACC high and ACC low, Fig. 5) agree with the S4 data. This illustrates a limit of this method to estimate particle settling velocities.

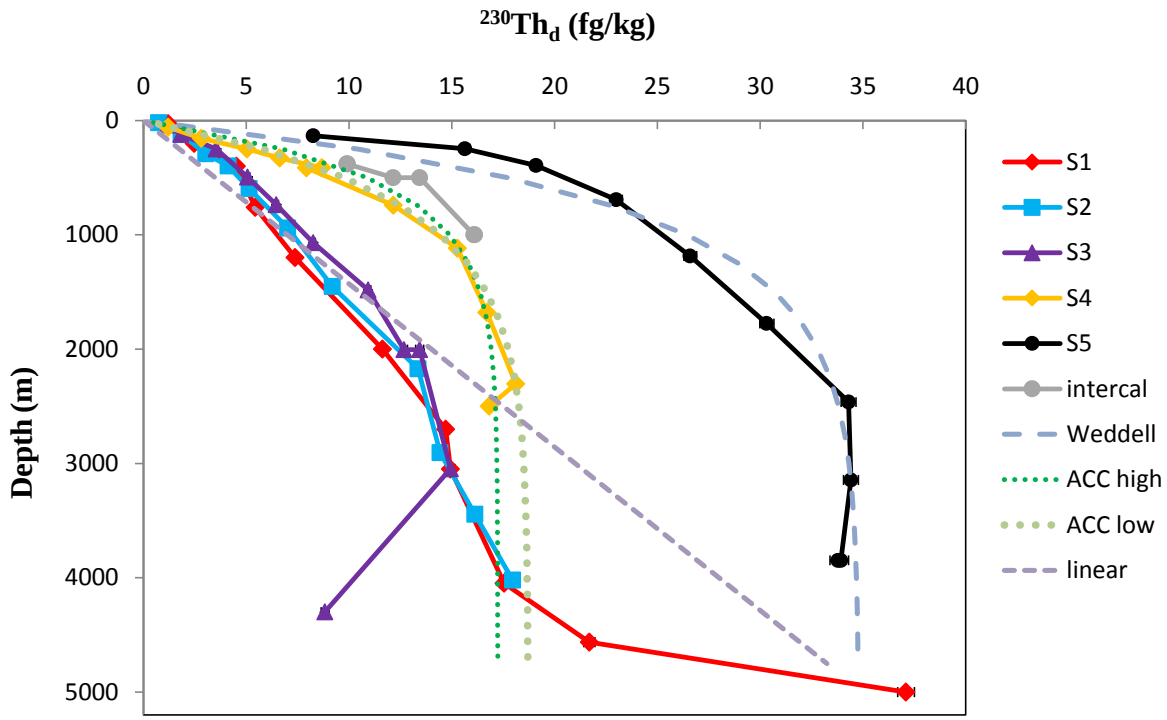

Fig. 5. Modelling of the Bonus Good Hope profiles. The dotted and dashed curves are calculated with Eq. 4. Weddell: C_i = 24 fg/kg, w_p = 875 m/y, τ_w = 20 y and K = 0.04. ACC low: C_i = 12 fg/kg, w_p = 803 m/y, τ_w = 12 y and K = 0.07. ACC high: C_i = 15 fg/kg, w_p = 1785 m/y, τ_w = 4 y and K = 0.125. linear: C_i = 0 fg/kg, w_p = 800 m/y, τ_w = + ∞ and K = 0.1.

This advection-scavenging model has been largely used to describe the vertical distribution of ^{230}Th in the Southern Ocean (Coppola et al., 2006, Venchiarutti et al., 2011, Rutgers van der Loeff et al., 2016). Despite crude assumptions (e.g., uniform influence throughout the water column by a single water mass), this mixing-scavenging model has the great merit of highlighting the impact of upwelling on $^{230}Th_d$ profiles and to provide an estimate of the particle settling speed when the 1D production-scavenging model cannot be used. Nevertheless, this model cannot fully describe the upwelling and mixing of 2 different water masses along an isopycnal surface as observed during BGH and described in the next section. Salinity data help to illustrate this point. For a conservative tracer (P_d = 0, w_p = 0 and C_p = 0) and assuming steady state, equation (3) reduces to:

$$\left(S_{t\_i} - S_t\right) = 0 \qquad (5)$$

This expresses that salinity is constant and equal to the salinity of the inflowing water ($S_t = S_{t\_i}$). In this model, LCDW is advected at all levels in the Weddell Gyre. It implies that the Weddell Gyre must be filled only with LCDW. Nevertheless, the $^{230}Th_t$ concentration in the Weddell

Gyre changes with depth due to the scavenging transport of $^{230}Th_t$ by sinking particles. Hence, this mixing-scavenging model cannot represent the mixing of water masses with different origins and labeled with different θ and S signatures as they are observed along the BGH section and elsewhere in the Southern Ocean. In principle, general circulation models, associated or coupled with biogeochemical model, have the potential to reproduce the coupled effect of scavenging and mixing, but the present generation of coupled models do not accurately describe the vertical distribution of scavenging intensity (e.g.: Dutay et al., 2009, Gu and Liu, 2017, Van Hulten et al., 2018).

4.2. Th isotopes along neutral density surfaces

While there are large horizontal concentration gradients of $^{230}Th_d$ and total (dissolved + ¨particulate) ^{230}Th ($^{230}Th_t$) along the BGH section (mostly between station S3 to S5, Fig 3), $^{230}Th_t$ concentration gradients are small on a given neutral density surface (Fig. 6). Figure 6 highlights that distribution of $^{230}Th_d$ is mainly driven by transport from upwelling and mixing along isopycnal surfaces. There is more variability of $^{232}Th_d$ or $^{232}Th_t$ (dissolved + particulate ^{232}Th) on a given neutral density value, presumably because large lithogenic inputs occur at stations S1 and S2 (Fig. 6).

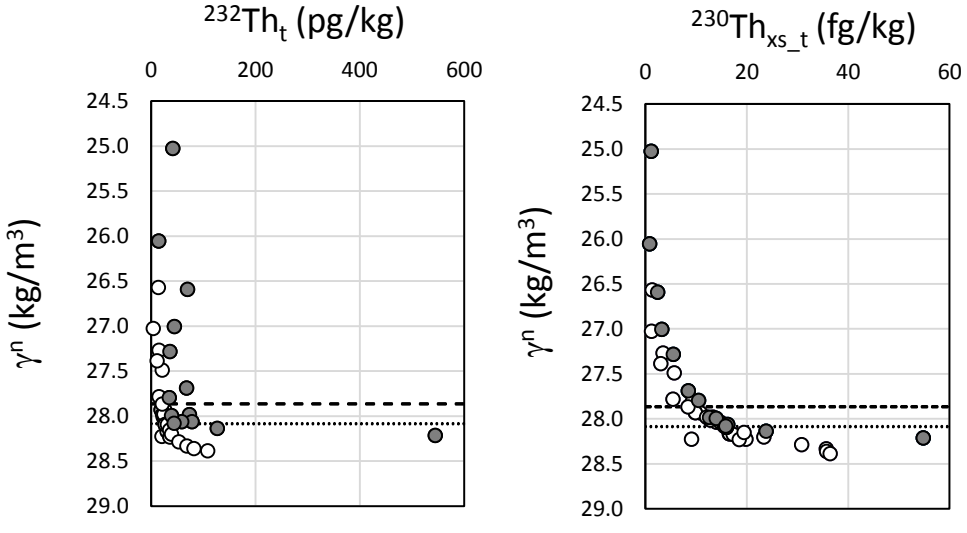

Fig. 6. Neutral density versus $^{232}Th_t$ and $^{230}Th_t$ concentration. Grey dots: S1 and S2 stations with high $^{232}Th_t$ contents. White dots: S3, S4 and S5. Dashed line: γ^n = 27.865 kg/m^3. Dotted line: γ^n = 28.094 kg/m^3.

In the following, we discuss concentration changes along isopycnal surfaces. As these changes are small, we restrict this discussion to the Bonus GoodHope data, all generated in the same laboratory, in order to avoid the systematic inter-laboratory differences identified during the GEOTRACES intercalibration (Anderson et al., 2012).

We focus on 2 neutral density surfaces: γ^n = 27.865 kg/m^3 and γ^n = 28.094 kg/m^3 (Fig ES2). The neutral density surface γ^n = 27.865 kg/m^3 can be followed from z=1500 m at station S1 to z=139 m at station S5. It crosses the following water masses: I-UCDW (S1), A-UCDW (S2 and S3), DP-UCDW (S4) and AASW/WW (S5). The neutral density surface: γ^n = 28.094 kg/m^3 can be followed from z = 3000 m at station S1 to z = 200 m at station S5. It is close to the neutral density of the deep salinity maximum observed in 2004 along the same section (Gladyshev et al., 2008). It crosses the following water masses: SE-NADW (S1 and S2), SW-NADW/AABW (S3), LCDW (S4) and AASW/WW (S5).

We choose these two neutral density surfaces because: (1) they are found along the whole section, (2) samples along these surfaces tend to form a linear trend on a θ-S diagram, indicating a binary mixing (Fig. 7), and (3) they are not interrupted by the Agulhas Ridge. When, at a given station, no sample was collected exactly on the selected neutral density surface, concentrations were linearly interpolated between the samples collected just above and below this surface at the same station. When the particulate Th was not analyzed with *in situ* pump samples at the target depth or in its vicinity (e.g., intercal station), we used the $^{232}Th_p$ concentration obtained with the Niskin filtration profiles and the $^{230}Th_p$ was calculated with the ($^{230}Th_p/^{232}Th_p$) ratio linearly interpolated between the ratios measured on particles just above and below or at the nearby station:

$$^{230}Th_{p\text{-estimates}} = {}^{232}Th_{p\text{-Niskin filtration}} * (^{230}Th_p/^{232}Th_p)_{interpolated} \quad (6)$$

$\underline{\gamma^n = 27.865}$ kg/m^3

On a θ-S diagram, S1, S2, S3 and S4 plot along a straight line, suggesting a binary mixing between S1 and S4 (Fig. 7a). S5 does not fall on this line, possibly due to ocean-atmosphere interactions (Abadie et al., 2017), so that this station does not correspond to the same binary mixing along this neutral density surface. Therefore, in the following, we will apply the mixing model mostly between stations S1 and S4 for this isopycnal.

On a S- $^{232}Th_t$ diagram, the stations S2 and S3 stand below the conservative mixing line between S1 and S4 (Fig. 7c). It corresponds to a depletion (net removal of ^{232}Th on sinking particles) of

515 $^{232}Th_t$ compared to a conservative mixing between S1 and S4: $\Delta^{232}Th_t<0$. The strong $^{232}Th_t$
516 inputs from the South African margin to the ACC are marked by a strong $^{232}Th_t$ concentration
517 gradient ($^{232}Th_t$ decrease by a factor ~4 between stations S1 and S4). A small $^{232}Th_t$ gradient
518 between Station S5 and S4 suggests smaller inputs from the Weddell Sea.
519
520 On a S- $^{230}Th_t$ diagrams, there is much less change in $^{230}Th_t$ concentration (~ 30% between
521 stations S1 and S4) compared to $^{232}Th_t$ presumably because the margin is not a strong source of
522 $^{230}Th_t$ for the ACC. Nevertheless, the $^{230}Th_t$ concentrations generally decrease southward.
523 However, stations S2 and S3 stand above the conservative mixing line between S1 and S4 (Fig.
524 7e). This trend would correspond to an excess of $^{230}Th_t$ compared to a conservative mixing
525 between S1 and S4: $\Delta^{230}Th_t>0$. There is an accumulation of ^{230}Th due to *in situ* production
526 despite the net removal of $^{232}Th_t$ during the same mixing process.
527
528 γ^n =28.094 kg/m^3
529 On a θ-S diagram, S3, S4, intercal and S5 plot along a straight line, suggesting a binary
530 mixing between S3 and S5 (Fig. 7b). S1 and S2 do not fall on this line, so that these 2 stations
531 do not correspond to the same binary mixing along this neutral density surface. Therefore, in
532 the following, we will restrict our analysis to stations S3 to S5 and, in the next section, we will
533 apply the mixing model only between stations S3 and S5.
534 On a S-$^{232}Th_t$ diagram, we observe the same trend as on the previous isopycnal: a strong
535 $^{232}Th_t$ decrease from S1 to S3 and a weaker decrease from S5 to S4 (Fig 7d). This illustrates the
536 role of the margins (and particularly the South African margin) as sources of ^{232}Th for the ACC.
537 We argued in the previous paragraph that waters from stations S1 and S2 do not seem directly
538 involved in the mixing observed further south. However, high $^{232}Th_t$ concentrations are also
539 observed in the SW-NADW sampled upstream of the BGH section. These high values are
540 acquired as this water flows along the Namibian margin (Scholten et al., 2008) so that it could
541 be a suitable $^{232}Th_t$ source fueling the southern part of the BGH section. S4 and intercal stations
542 stand below the S3-S5 binary mixing line, reflecting $^{232}Th_t$ depletion at these 2 stations
543 compared to conservative mixing, expressed as $\Delta^{232}Th_t<0$ (Fig 7). More generally, paired
544 $^{232}Th_t$–S data indicates that there is a net Th removal by the settling particles while water masses
545 mix between stations S3 and S5.
546

As for γ^n =27.865 kg/m^3, the relative variations of $^{230}Th_t$ are small (Fig. 7f). On a S-$^{230}Th_t$ diagram, the S4 and intercal stations stand above the S3-S5 binary conservative mixing trend (S1 and S2 are not considered because they are not involved in the mixing on this isopycnal). This trend would correspond to an excess of $^{230}Th_t$ compared to a conservative mixing: $\Delta^{230}Th_t>0$. Like on the previous isopycnal, ^{230}Th accumulates due to *in situ* production despite the net removal of $^{232}Th_t$ during water mass mixing.

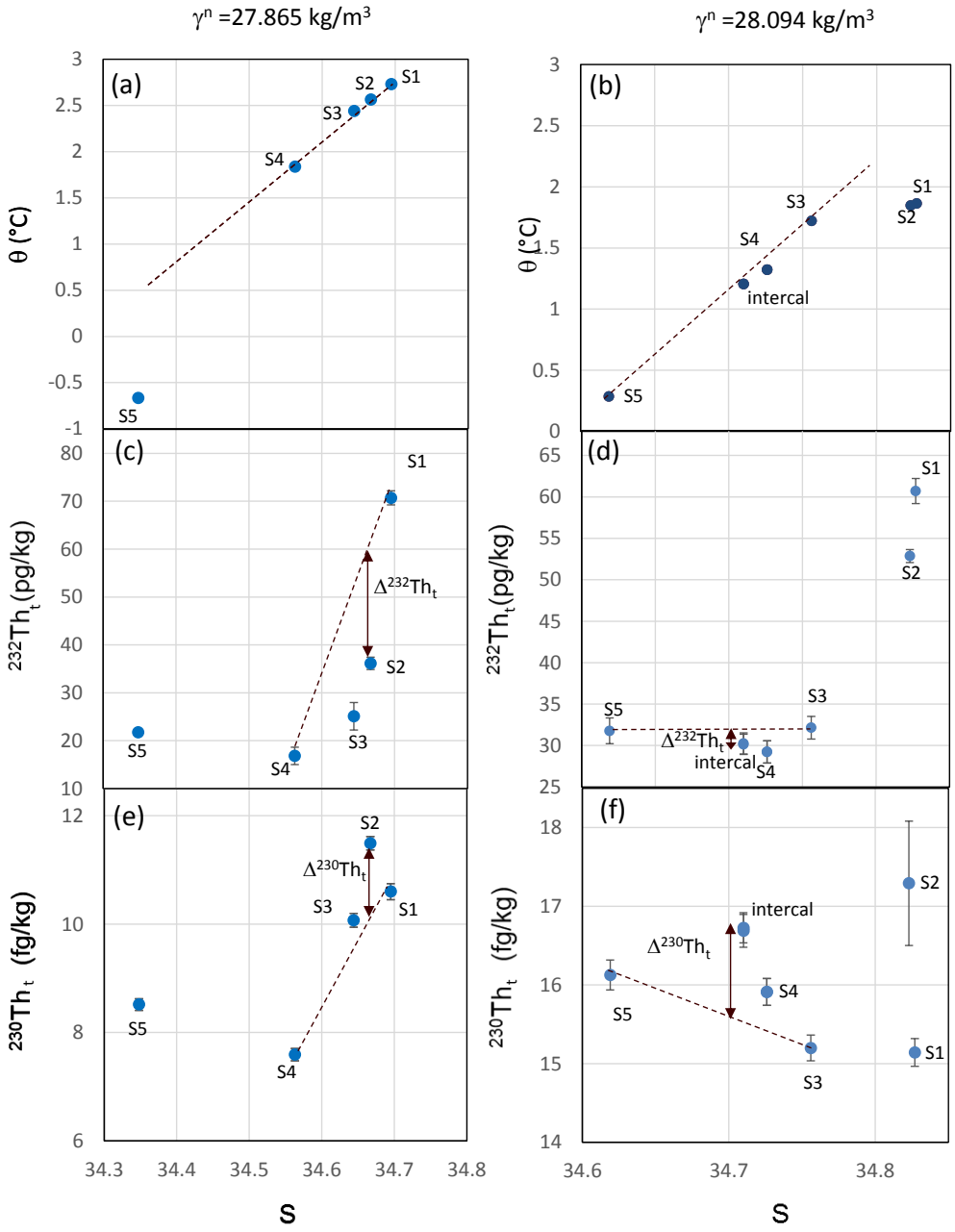

Figure 7: Potential temperature, $^{232}Th_t$ and $^{230}Th_t$ versus salinity on different neutral density surfaces. Left: γ^n =27.865 kg/m^3. Right: γ^n =28.094 kg/m^3. a-b: Potential temperature versus salinity. c-d: $^{232}Th_t$

versus salinity. e-f: $^{230}Th_t$ versus salinity. Thin dashed line: conservative binary mixing line. Vertical double arrows denote the deviation compared to conservative mixing.

See table ES3 for the data calculated on isopycnals.

4.3. Modeling advection-diffusion-scavenging along a neutral density surface.

In the deep ocean, water mass mixing is thought to occur preferentially along isopycnal surfaces. There is both advection and eddy diffusion along the steep isopycnal surfaces of the Southern Ocean (Zika et al., 2009, Naveira Garabato et al., 2007). While diapycnal mixing is important in the Drake Passage due to the rough topography, it appears to be much weaker out of the passage (Watson et al., 2013), so we will neglect it for the present analysis. We approximate the combined effect of advection and diffusion along an isopycnal by extending the conservation equation (2) with the explicit introduction of advection and diffusion terms in an infinitesimal volume of water at steady state (Jenkins, 1987):

$$K_i \frac{\partial^2 C_t}{\partial x^2} - u_i \frac{\partial C_t}{\partial x} + P_d - w_p \left(\frac{\partial C_p}{\partial z}\right) = 0 \qquad (7)$$

Where C_t is the total (dissolved + particulate) concentration of the tracer, C_p the particulate concentration of the tracer, K_i is the cross-stream isopycnal eddy diffusion coefficient and u_i is the cross-stream isopycnal advection velocity. The x-axis is parallel to the isopycnal surface in the meridional direction and oriented northward. The z axis is oriented perpendicular to the isopycnal surface and hence is almost vertical. Just like in the advection-scavenging model (equ. 3), keeping w_p out of the partial derivative with respect to z (writing $w_p \left(\frac{\partial C_p}{\partial z}\right)$ instead of $\left(\frac{\partial (w_p C_p)}{\partial z}\right)$) requires to assume that w_p does not vary with z. We integrate Eq. 7 along isopycnal surfaces of the BGH section between the stations corresponding to the end members of water mass mixing (stations for S1 and S4 for γ^n =27.865 kg/m^3 and S3 and S5 for γ^n =28.094 kg/m^3). Unlike most Th models that are built by vertically integrating the conservation equation, here we integrate the conservation equation along surfaces that are only slightly tilted relative to the horizontal. This is a simplified view of water transport because while water moves across the ACC, it is also rapidly advected eastward by the ACC (S2-S4) and the northern limb of the Weddell Gyre (S5). We assume that K_i, u_i, w_p and (dC_p/dz) are all constant along x in order to obtain analytical solutions. We note $C_t = C_{t\text{-conc}} + \Delta C_t$, where $C_{t\text{-conc}}$ is the concentration of the tracer if it had a conservative behavior and ΔC_t (as plotted in Fig 7) is the deviation of this tracer compared to a conservative behavior. The solution is then:

$$C_{t-conc} = \frac{e^{\frac{u_i}{K_i}x} - e^{\frac{u_i}{K_i}x_B}}{e^{\frac{u_i}{K_i}x_A} - e^{\frac{u_i}{K_i}x_B}}\left(C_{t\_A} - C_{t\_B}\right) + C_{t\_B} \quad (8)$$

$$\Delta C_t = \frac{\left(P_d - w_p\frac{dC_p}{dz}\right)}{u}\left((x - x_B) + (x_B - x_A)\left(\frac{e^{\frac{u_i}{K_i}x} - e^{\frac{u_i}{K_i}x_B}}{e^{\frac{u_i}{K_i}x_A} - e^{\frac{u_i}{K_i}x_B}}\right)\right) \quad (9)$$

Here A and B represent stations S1 and S4 or S3 and S5 along the neutral density surface. For a conservative tracer such as salinity, the concentration is given by:

$$S = \frac{e^{\frac{u_i}{K_i}(x - x_A)} - 1}{e^{\frac{u_i}{K_i}(x_B - x_A)} - 1}(S_B - S_A) + S_A \quad (10)$$

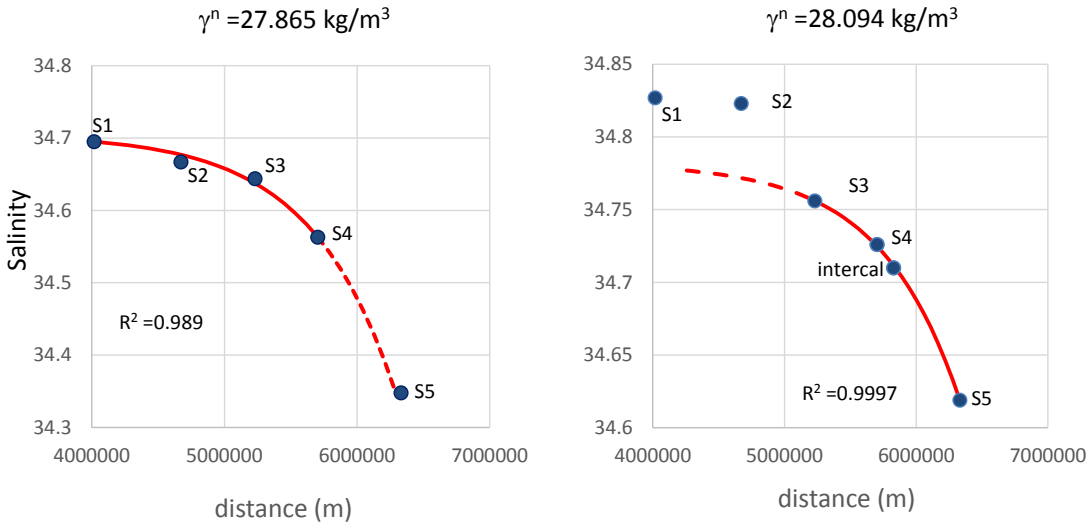

Figure 8: Advection-diffusion modelling of salinity. The distance considered is the meridian distance from the equator (d = 0 at the equator). Red curves are obtained with equation 10. u_i/K_i is adjusted by least squares just based on the stations corresponding to the 2-water mass mixing and by forcing the curves to pass through the 2 water mass end members. The values of u_i/K_i are given in Table 1. Dotted curves are extrapolated to the rest of the section but the corresponding stations are not used to calculate the curve parameters.

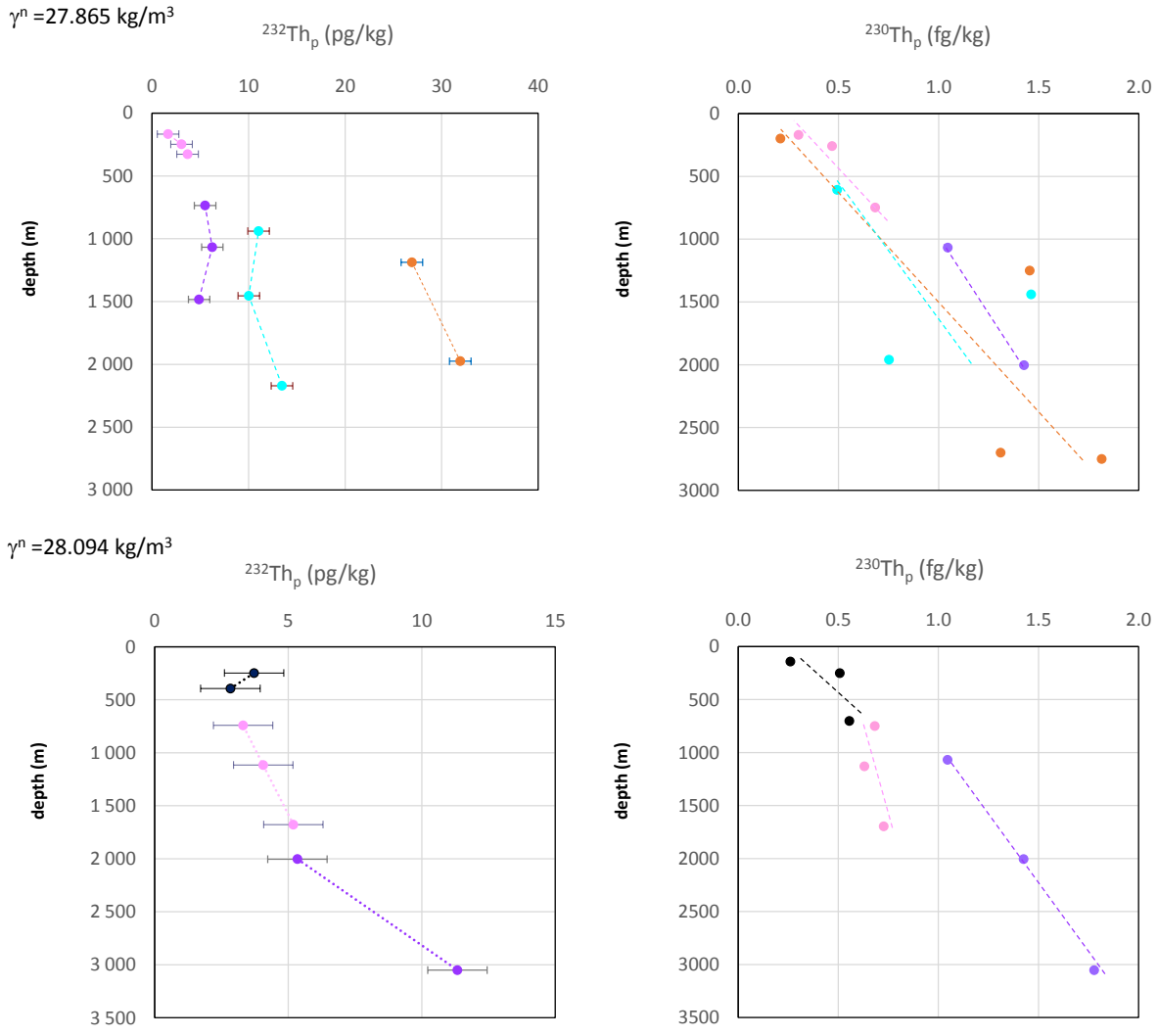

Figure 9: $^{232}Th_p$ and $^{230}Th_p$ profiles. For each isopycnal, we also plot the sample analyzed just above and below in order to define the slopes ($d^{232}Th_p/dz$) and ($d^{230}Th_p/dz$), respectively. Color code is the same as in Figure 3.

$\underline{\gamma^n = 27.865}$ kg/m^3

Equation 10 allows determining the u_i/K_i ratio using salinity data along the BGH section. For γ^n = 27.865 kg/m^3, we obtain u_i/K_i = - 1.57×10^{-6} m^{-1} (Fig. 8, Tab. 1). The minus sign corresponds to a southward advection (u_i <0 and K_i is always positive). This is consistent with the southward upwelling expected based on the average circulation of UCDW in the Southern Ocean within this density range (section 2.1). This feature is observed for the 2 isopycnals studied here (see below for γ^n = 28.094 kg/m^3).

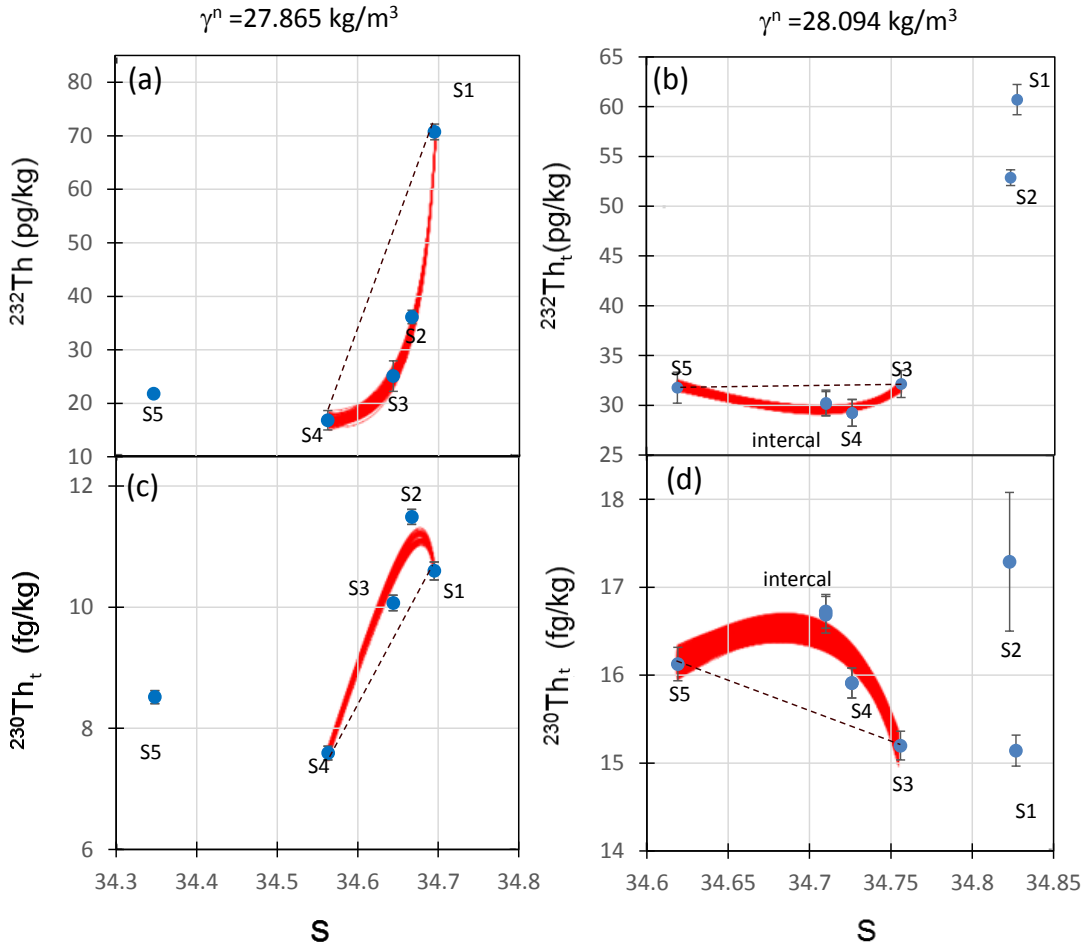

Figure 10: Advection-diffusion modelling of S and Th_t isotopes compared to data. Staked red curves: modelled curves with the highest R^2 values (Tab. 1). Thin black dotted line: conservative mixing between S3 and S5.

Tab. 1: Model parameters and outputs.

	$d^{232}Th_p/dz$ (pg/kg/m)	$d^{230}Th_p/dz$ (fg/kg/m)	u_i/K_i (m^{-1})	K_i (m^2/s)	u_i (m/s)	w_p (m/y)	R^2_0	R^2_2
γ^n = 27.865 kg/m^3	- 0.001 / + 0.012	3.8×10^{-4} - 6.2×10^{-4}	-1.57×10^{-6}	2000 ±840	- 0.0033 ± 0.0014	674±250	~ 0.945	~ 0.994
γ^n = 28.094 kg/m^3	+ 0.001 / + 0.009	0.4×10^{-4} - 3.5×10^{-4}	-1.65×10^{-6}	2180 ±480	- 0.0036 ± 0.0008	418±470	~ 0.806	~ 0.696

To determine $d^{232}Th_p/dz$, we use the Niskin filtration data because they have a better vertical resolution. We determine $d^{232}Th_p/dz$ based on the $^{232}Th_p$ concentrations measured above and

below the depth of the neutral density surface at each station (Fig. 9). For γ^n = 27.865 kg/m^3, $d^{232}Th_p/dz$ varies strongly between S1 and S4. Interestingly, we obtain low $d^{232}Th_p/dz$ values when the $^{232}Th_t$ horizontal gradient is low (e.g., $d^{232}Th_p/dz$ = - 0.001 pg/kg/m at S3) and higher $d^{232}Th_p/dz$ values when the $^{232}Th_t$ horizontal gradient is high (e.g., $d^{232}Th_p/dz$ = + 0.006 pg/kg/m at S1). In other words, the increase of $^{232}Th_t$ with depth is due to the horizontal transport of ^{232}Th by eddy diffusion from the margin, whereas without inputs from the margins the dissolved and particulate ^{232}Th concentration would be expected to be constant with depth (Roy-Barman et al., 1996). Ideally, it would be best to integrate equation 7 with $d^{232}Th_p/dz$ and $d^{230}Th_p/dz$ varying with x. In practice, it is difficult to determine the evolution of these gradients along the isopycnal or even to determine the exact average gradients between stations S1 and S4. As a first approach, we will just use the range of the gradients measured between S1 and S4 as input values to determine w_p, u_i and K_i. For ^{232}Th, we use a range $d^{232}Th_p/dz$ from - 0.001 to + 0.012 pg/kg/m (Fig. 9, Tab. 1). For ^{230}Th, most $^{230}Th_p$ data plot along a slope ranging between 3.8×10^{-4} fg/kg/m and 6.2×10^{-4} fg/kg/m (Fig. 9, Tab. 1).

We then estimate w_p and u_i with a least square approach. Using Monte Carlo simulations, we maximize the coefficient of determination (R^2) of the $^{230}Th_t$ versus S and $^{232}Th_t$ versus S curves simultaneously. In equation 9, w_p and the dTh_p/dz terms are present as products so that their opposite variations cancel each other. As a consequence, a relatively large range of w_p, $d^{230}Th_p/dz$ and $d^{232}Th_p/dz$ values yield similar R^2 values. Therefore, we report w_p and u_i obtained for a range of high R^2 values. We obtain w_p = 674 ± 250 m/y and u_i = - 0.0033 ± 0.0014 m/s. Using the u_i/K_i ratio estimated previously, we deduce K_i = 2000 ± 840 m/s^2.

$\underline{\gamma^n = 28.094}$ kg/m^3

For γ^n = 28.094 kg/m^3, most of the $^{230}Th_p$ data plot along a slope of 5×10^{-4} fg/kg/m, whereas $^{232}Th_p$ data plot along a slope of 2×10^{-4} pg/kg/m (Fig. 10). In both diagrams, the slope of the S4 station is poorly defined and potentially lower than the average. Using the same method, we obtain $u_i/K_i = -1.65\times10^{-6}$ m^{-1}, w_p = 435 ± 324 m/y, u_i = - 0.0036 ± 0.0008 m/s and K_i = 2180 ± 480 m/s^2 (Fig 8-9, Tab. 1).

The 2 K_i values estimated here are on the upper end of the range (300 to 1800 m^2/s) reported in the Southern Ocean, whereas u_i is on the lower but of the same order of magnitude than an

666 estimate of the cross-stream horizontal velocity associated with the upwelling in the ACC (~ -
667 0.010 ± 0.003 m/s, Naveira Garabato et al., 2007, Zika et al., 2009).
668
669 We have estimated w_p at relatively close depths on the 2 isopycnals (1200-1500 m for γ^n =
670 27.865 kg/m^3 at stations S3 and S2 and 1000-1200 m for γ^n = 28.094 kg/m^3 at stations intercal
671 and S4, Fig. ES2). Taking the corresponding w_p at face value (but keeping in mind that they
672 strongly rely on the particulate concentration gradient estimate), it seems that there is a
673 southward decrease of w_p (for γ^n = 27.865, w_p = 600 m/y and for γ^n = 28.094 kg/m^3, w_p = 300
674 m/y). This southward decrease of settling speed seems consistent with the ^{238}U-^{234}Th
675 disequilibrium in the surface waters that decreased from the north to the south of the polar
676 front zone (PFZ) during the BGH cruise (Planchon et al., 2013) and 2 weeks earlier on the
677 same transect during the ANTXXIV/3 cruise (Rutgers van der Loeff et al., 2011). This
678 gradient of the ^{238}U-^{234}Th disequilibrium indicates a higher removal rate of ^{234}Th and suggests
679 a higher particle settling velocity in the north compared the south of the PFZ.
680
681 It is rewarding that the particle settling speeds obtained with the isopycnal mixing model
682 (which does not integrate the conservation equation over the water column) are in the range of
683 the speeds generally obtained with the vertical 1D model (see section 4.1; Rutgers van der
684 Loeff and Berger, 1993). In the 1D production-scavenging model, w_p is given by (see section
685 4.1.): $w_p = P/(d^{230}Th_p/dz)$. However, w_p is usually obtained by averaging ($d^{230}Th_p/dz$) over
686 the whole water column or a large part of the water column as we did in section 4.1.
687 Consequently, the w_p does not depend on sharp changes of ($d^{230}Th_p/dz$) that could result from
688 random errors on $^{230}Th_p$ at intermediate depths. In the 1D mixing-scavenging model some
689 advection is introduced but the model is still integrated from the surface to the seafloor, so
690 that random errors on $^{230}Th_p$ tend to be smoothed out (Rutgers van der Loeff and Berger,
691 1993). In addition, ^{234}U *in situ* decay is not the only source of dissolved ^{230}Th, because
692 advection also brings dissolved and particulate ^{230}Th, which adds up uncertainty on the input
693 rate of ^{230}Th.
694 In the isopycnal mixing model presented here, the uncertainties cited above can have much
695 larger effects on w_p because i) ($d^{230}Th_p/dz$) is calculated over much thinner depth ranges and
696 ii) combined effects of high water flow rates and small ^{230}Th concentration gradients implies
697 that the net effect of circulation on ^{230}Th transport is subject to large relative uncertainties.
698 Nevertheless, the isopycnal mixing model opens the possibility to calculate the vertical

699 evolution of w_p in highly dynamical environments where the hypotheses of the 1D model are
700 clearly not fulfilled.
701

702 In a recent series of paper, non-linear dissolved ^{230}Th profiles are modelled with a
703 purely 1D approach by adjusting adsorption/desorption/remineralization rates and particle
704 settling velocities that are assumed to vary with depth (Lerner et al., 2016, 2017 and 2018).
705 These numerous parameters are adjusted by using different Th isotopes (^{228}Th, ^{230}Th, ^{234}Th).
706 This approach is different but not inconsistent with our approach because: (1) Unlike the
707 present paper, Lerner et al focus on areas where advection and eddy diffusion are expected to
708 be negligible; (2) In the present paper, we make no hypothesis on the processes driving
709 dissolved-particulate transfers (Eq. 7). Ultimately, it should be possible to determine
710 adsorption/desorption rates in areas with weak currents and then to use these values in regions
711 with a vigorous circulation such as the ACC. Lerner's approach treats explicitly the case of w_p
712 varying with depth, whereas our approach to leave the possibility to determine the particle
713 settling speed at different depths/density. To do so rigorously, it will be necessary to treat w_p
714 like a parameter varying with depth (see section 4.3).

715

716 5. Conclusion

717 While we still used crude approximations, the model proposed here opens the
718 possibility to determine the particle settling speed and to bring constraints on the isopycnal
719 mixing rate at different vertical levels and with a more realistic description of the vertical
720 structure of the water column. The improvement that will come out of the method proposed
721 here will require sampling with higher horizontal and vertical sampling resolutions, a goal
722 partly achieved in the framework of the GEOTRACES program. It also requires progresses
723 for the particulate Th analysis and constant efforts for the intercalibration of the different
724 cruises.
725
726
727
728
729

Acknowledgements:

The authors would like to thank S. Speich and M. Boyé, the chief scientists of the BGH cruise, and the crew of the research vessel Marion Dufresne II (IPEV). We acknowledge Christophe Guillerm, Lionel Scouarnec, Thomas Arsouze and Amandine Radic for the sample collection on board. We are grateful to the 2 anonymous reviewers who improved the manuscript with their very helpful comments. Support provided by the ANR (Programme Blanc 2007: ANR- 07-BLAN-0146-02) and the INSU/CNRS (programme INSU/LEFE-CYBER) is gratefully acknowledged.

References :

Abadie, C., Lacan, F., Radic, A., Pradoux, C., Poitrasson, F., 2017. Iron isotopes reveal distinct dissolved iron sources and pathways in the intermediate versus deep Southern Ocean. Proceedings of the National Academy of Sciences, 114(5), 858-863.

Anderson, R.F., Fleisher, M.Q., Robinson, L.F., Edwards, R.L., Hoff, J. a., Moran, S.B., Loeff, M.R. Van Der, Thomas, A.L., Roy-Barman, M., Francois, R., 2012. GEOTRACES intercalibration of ^{230}Th, ^{232}Th, ^{231}Pa, and prospects for ^{10}Be. Limnol. Oceanogr. Methods 10, 179–213.

Arhan, M., Mercier, H., Park, Y.-H., 2003. On the Deep Water circulation of the eastern South Atlantic Ocean. Deep-Sea Research Part I 50, 889–916.

Bacon, M.P., Anderson, R.F., 1982. Distribution of Thorium isotopes between dissolved and particulate forms in the deep sea. J. Geophys. Res. 87, 2045–2056. doi:10.1029/JC087iC03p02045

Bown, J., Boye, M., Baker, A., Duvieilbourg, E., Lacan, F., Le Moigne, F., ... Nelson, D. M., 2011. The biogeochemical cycle of dissolved cobalt in the Atlantic and the Southern Ocean south off the coast of South Africa. Marine Chemistry 126, 193-206.

Chever, F., Bucciarelli, E., Sarthou, G., Speich, S., Arhan, M., Penven, P., Tagliabue, A., 2010. Physical speciation of iron in the Atlantic sector of the Southern Ocean along a transect from the subtropical domain to the Weddell Sea Gyre. Journal of Geophysical Research: Oceans, 115(C10).

Chase, Z., Anderson, R. F., Fleisher, M. Q., Kubik, P. W., 2003. Scavenging of ^{230}Th, ^{231}Pa and ^{10}Be in the Southern Ocean (SW Pacific sector): The importance of particle flux, particle composition and advection. Deep Sea Research Part II: Topical Studies in Oceanography 50, 739-768.

Coppola, L., Roy-Barman, M., Mulsow, S., Povinec, P., Jeandel, C., 2006. Thorium isotopes as tracers of particles dynamics in the Indian sector of the Southern Ocean. Marine Chemistry 100, 299-313

Dutay, J.-C., Lacan, F., Roy Barman, M. and Bopp, L., 2009. The influence of particle size and type on ^{231}Pa and ^{230}Th simulation with a global coupled biogeochemical- ocean general circulation model: a first approach. G-cubed, doi:10.1029/2008GC002291

Garcia-Solsona, E., Jeandel, C., Labatut, M., Lacan, F., Vance, D., Chavagnac, V., Pradoux, C., 2014. Rare earth elements and Nd isotopes tracing water mass mixing and particle-seawater interactions in the SE Atlantic. Geochimica et Cosmochimica Acta, 125, 351-372.

Gdaniec, S., Roy-Barman, M., Foliot, L., Thil, F., Dapoigny, A., Burckel, P, A. Masque, P., Garcia-Orellana, J., Morth, M., Andersson, P. S., 2018. Thorium and protactinium isotopes as tracers of marine particle fluxes and deep water circulation in the Mediterranean Sea. Marine Chemistry 199, 12-23.

Gdaniec, S., Roy-Barman, M., Levier, M., Valk O., Rutgers van der Loeff, M., Foliot, L., Dapoigny, A., Morth, M., Andersson, P. S., 2019. ^{231}Pa and ^{230}Th in the Arctic Ocean: implications for Boundary Scavenging and ^{231}Pa-^{230}Th fractionation in the Eurasian Basin. Submitted to Chemical Geology

Gladyshev S., Arhan M., Sokov A., Speich S., 2008. A hydrographic section from South Africa to the southern limit of the Antarctic Circumpolar Current at the Greenwich meridian. Deep-Sea Res. I 55, 1284–1303.

Gu, S., Liu, Z., 2017. ^{231}Pa and ^{230}Th in the ocean model of the Community Earth System Model (CESM1.3), Geosci. Model Dev., 10, 4723-4742

Jeandel, C., Venchiarutti, C., Bourquin, M., Pradoux, C., Lacan, F., van Beek, P., Riotte, J., 2011. Single column sequential extraction of Ra, Nd, Th, Pa and U from a natural sample. Geostand. Geoanalytical Res. 35, 449–459.

Jenkins, W. J., 1987. ^{3}H and ^{3}He in the Beta Triangle: Observations of gyre ventilation and oxygen utilization rates. J. Phys. Oceanogr. 17, 763-783.

Lerner, P., Marchal, O., Lam, P. J., Anderson, R. F., Buesseler, K., Charette, M. A., Edwards, R. L., Hayes, C. T., Huang, K. F., Lu, Y., Robinson, L. F., Solow, A., 2016. Testing models of thorium and particle cycling in the ocean using data from station GT11-22 of the US GEOTRACES North Atlantic Section, Deep Sea Research Part I: Oceanographic Research Papers, 113, 57–79.

Lerner, P., Marchal, O., Lam, P. J., Buesseler, K., Charette, M., 2017. Kinetics of thorium and particle cycling along the US GEOTRACES North Atlantic Transect. Deep Sea Research Part I: Oceanographic Research Papers, 125, 106-128.

Lerner, P., Marchal, O., Lam, P. J., Solow, A., 2018. Effects of particle composition on thorium scavenging in the North Atlantic. Geochimica et Cosmochimica Acta, 233, 115-134.

Marshall, J., Speer, K., 2012. Closure of the meridional overturning circulation through Southern Ocean upwelling. Nature Geoscience 5, 171-180.

Naveira Garabato, A.C., Stevens, D.P., Watson, A.J. and Roether, W., 2007. Short-circuiting of the overturning circulation in the Antarctic Circumpolar Current. Nature 447|, 194-197.

Nozaki, Y., Horibe, Y., Tsubota, H., 1981. The water column distribution of thorium isotopes in the western North Pacific, Earth Planet. Sc. Lett., 54, 203–216.

Planchon, F., Cavagna, A. J., Cardinal, D., André, L., Dehairs, F., 2013. Late summer particulate organic carbon export and twilight zone remineralisation in the Atlantic sector of the Southern Ocean. Biogeosciences 10, 803-820.

Planquette, H., Sherrell, R. M., 2012. Sampling for particulate trace element determination using water sampling bottles: methodology and comparison to in situ pumps. Limnology and Oceanography: methods 10, 367-388.

Roy-Barman, M., 2009. Modelling the effect of boundary scavenging on Thorium and Protactinium profiles in the ocean. Biogeosciences 6, 7853–7896.

Roy-Barman, M., Chen, J.H., Wasserburg, G.J., 1996. The sources and the fates of thorium. Earth Planet. Sci. Lett. 139, 351–363.

Roy-Barman, M., Coppola, L., Souhaut, M., 2002. Thorium isotopes in the western Mediterranean Sea: An insight into the marine particle dynamics. Earth Planet. Sci. Lett. 196, 161–174.

Rutgers van der Loeff, M.M., Berger, G.W., 1993. Scavenging of ^{230}Th and ^{231}Pa near the antarctic polar front in the South Atlantic. Deep. Res. Part I 40, 339–357

Rutgers van der Loeff, R., Cai, P. H., Stimac, I., Bracher, A., Middag, R., Klunder, M. B., & van Heuven, S. M., 2011. ^{234}Th in surface waters: distribution of particle export flux across the Antarctic Circumpolar Current and in the Weddell Sea during the GEOTRACES expedition ZERO and DRAKE. Deep Sea Research Part II: Topical Studies in Oceanography 58, 2749-2766.

Rutgers van der Loeff, M., Venchiarutti, C., Stimac, I., van Ooijen, J., Huhn, O., Rohardt, G., & Strass, V., 2016. Meridional circulation across the Antarctic Circumpolar Current serves as a double ^{231}Pa and ^{230}Th trap. Earth and Planetary Science Letters, 455, 73-84.

Schlitzer, R., 2007. Ocean data view. http://odv. awi. de.

Scholten, J. C., Fietzke, J., Mangini, A., Garbe-Schönberg, C. D., Eisenhauer, A., Schneider, R., Stoffers, P., 2008. Advection and scavenging: Effects on 230Th and 231Pa distribution off Southwest Africa. Earth and Planetary Science Letters, 271(1), 159-169.

Sims, K. W., Gill, J. B., Dosseto, A., Hoffmann, D. L., Lundstrom, C. C., Williams, R. W., ... Glessner, J. J., 2008. An inter-laboratory assessment of the thorium isotopic composition of synthetic and rock reference materials. Geostandards and Geoanalytical Research 32, 65-91.

Sokolov, S., Rintoul, S. R., 2009. Circumpolar structure and distribution of the Antarctic Circumpolar fronts: 1. Mean circumpolar path, J. Geophys. Res., 114, C11018, doi:10.1029/2008JC005108.

Thomas, A.L., Henderson, G.M., Robinson, L.F., 2006. Interpretation of the 231Pa/230Th paleocirculation proxy: new water-column measurements from the southwest Indian Ocean. Earth Planet. Sci. Lett. 241, 493.

van Hulten, M. M. P., Dutay, J. C., Roy-Barman, 2018. A global scavenging and circulation ocean model of thorium-230 and protactinium-231 with an improved particle dynamics (NEMO–ProThorP 0.1). Goescientific model development 11, 3537-3556.

Venchiarutti, C., Jeandel C., Roy-Barman, M., 2008. Particle dynamics in the wake of Kerguelen Island traced by thorium isotopes (Southern Ocean, KEOPS program). Deep Sea Research I 55, 1343-1363

Venchiarutti, C., van der Loeff, M.R., Stimac, I., 2011. Scavenging of ^{231}Pa and thorium isotopes based on dissolved and size-fractionated particulate distributions at Drake Passage (ANTXXIV-3). Deep. Res. Part II Top. Stud. Oceanogr. 58, 2767–2784.

Walter, H.J., Rutgers van der Loeff, M.M., Hoeltzen, H., 1997. Enhanced scavenging of ^{231}Pa relative to ^{230}Th in the South Atlantic south of the Polar Front: Implications for the use of the ^{231}Pa/^{230}Th ratio as a paleoproductivity proxy. Earth Planet. Sci. Lett. 149, 85–100.

Watson A. J., Ledwell J. R., Messias M. J., King B. A., Mackay N., Meredith M. P., Mills B., and Garabato A. C. N., 2013. Rapid cross-density ocean mixing at mid depths in Drake Passage measured by tracer release. Nature 501, 408–413.

Zika, J. D., Sloyan, B. M. & McDougall, T. J., 2009. Diagnosing the Southern Ocean overturning from tracer fields. J. Phys. Oceanogr. 39, 2926-2940.

Table ES1: Dissolved Thorium data.

Station	Depth (m)	θ (°C)	Salinity	γ^n (kg/m^3)	$^{232}Th_d$ [1] (pg/kg)	$^{230}Th_p$ [1] (pg/kg)	$^{230}Th_{p\text{-}xs}$ [2] (pg/kg)	Water mass
S1: 36.50°S, 13.10°E, 4923 m bottom depth								
	29	20.785	35.617	25.0222	34.7 ± 1.3	1.21 ± 0.03	1.06 ± 0.03	ICW
	198	12.364	35.014	26.53	52.1 ± 1.3	2.48 ± 0.04	2.25 ± 0.04	ICW
	397	9.824	34.757	26.7918	50.1 ± 1.5	4.52 ± 0.06	4.30 ± 0.06	ICW
	753	4.973	34.346	27.1602	37.2 ± 1.3	5.45 ± 0.08	5.29 ± 0.08	i-AAIW
	1188	3.279	34.551	27.5004	38.0 ± 1.3	7.38 ± 0.12	7.22 ± 0.12	i-AAIW
	1975	2.515	34.808	27.7752	40.2 ± 1.4	11.64 ± 0.18	11.46 ± 0.18	SE-NADW
	2664	2.132	34.838	27.8316	42.0 ± 1.3	14.71 ± 0.19	14.52 ±0.19	SE-NADW
	3005	1.945	34.836	27.8444	42.2 ± 1.4	14.94 ± 0.17	14.76 ± 0.17	SE-NADW
	3981	0.892	34.749	27.8506	70.0 ± 1.4	17.55 ± 0.23	17.25 ± 0.23	AABW
	4565	0.716	34.733	27.8493	69.1 ± 1.6	21.70 ± 0.27	21.40 ±0.27	AABW
	4907	0.568	34.72	27.8481	288.5 ± 3.5	37.10 ± 0.41	35.84 ± 0.41	AABW
S2: 42.47°S, 08.93°E, 4070 m bottom depth								
	20	12.951	34.521	26.0547	11.1 ± 1.4	0.74 ± 0.02	0.70 ± 0.03	ICW
	124	9.083	34.482	26.7815	19.8 ± 1.4	1.84 ± 0.03	1.75 ± 0.04	ICW
	292	6.654	34.267	27.0053	36.2 ± 1.3	3.04 ± 0.04	2.89 ± 0.04	ICW/a-AAIW
	398	6.01	34.292	27.1231	38.8 ± 1.5	4.13 ± 0.06	3.97 ± 0.06	ICW/a-AAIW
	595	4.138	34.185	27.2829	30.9 ± 1.4	5.14 ± 0.08	5.01 ± 0.08	a-AAIW
	940	3.075	34.313	27.5162	25.7 ± 1.3	7.02 ± 0.09	6.90 ± 0.09	a-AAIW
	1453	2.626	34.585	27.7945	26.1 ± 1.3	9.19 ± 0.11	9.07 ± 0.11	UCDW
	2172	2.346	34.79	27.994	31.1 ± 1.3	13.36 ± 0.16	13.22 ± 0.16	SE-NADW
	2905	1.967	34.827	28.0789	35.8 ± 1.3	14.43 ± 0.16	14.28 ± 0.16	SE-NADW
	3445	1.427	34.792	28.1359	36.9 ± 1.6	16.13 ± 0.24	15.96 ± 0.24	SE-NADW
	4021	0.81	34.741	28.1961	63.9 ± 1.5	17.96 ± 0.22	17.68 ± 0.22	AABW
S3: 47.55°S, 04.37°E, 4480 m bottom depth								
	40	6.32	33.733	26.5685	7.5 ± 1.4	1.19 ± 0.04	1.15 ± 0.04	AASW
	124	4.029	33.867	27.0072	8.3 ± 1.3	1.82 ± 0.04	1.79 ± 0.04	AASW
	248	3.633	34.101	27.2697	15.3 ± 1.4	3.55 ± 0.07	3.48 ± 0.07	AASW/a-AAIW
	495	2.739	34.233	27.4888	17.1 ± 1.2	5.07 ± 0.07	5.00 ± 0.07	a-AAIW
	742	2.591	34.407	27.6574	16.8 ± 1.3	6.46 ± 0.11	6.39 ± 0.11	a-AAIW/UCDW
	1068	2.447	34.575	27.8099	18.2 ± 1.3	8.26 ± 0.10	8.18 ± 0.10	A_UCDW
	1482	2.334	34.716	27.936	22.2 ± 1.5	10.93 ± 0.17	10.83 ± 0.17	SW-NADW
	2003	1.971	34.771	28.0376	23.2 ± 1.2	12.68 ± 0.15	12.58 ± 0.15	SW-NADW
	2003				23.2 ± 1.5	13.45 ± 0.16	13.34 ± 0.16	
	3052	0.955	34.731	28.1653	29.2 ± 1.6	14.94 ± 0.19	14.81 ± 0.19	SW-NADW
	4299	0.415	34.695	28.2262	18.5 ± 1.3	8.83 ± 0.12	8.75 ± 0.12	AABW

927 Table ES1 continued

S4: 51.85°S, 00.00°E, 2570 m bottom depth							
59	2.521	33.712	27.0277	4.7 ± 1.5	1.20 ± 0.03	1.18 ± 0.03	AASW
168	0.827	34.033	27.4838	10.8 ± 1.5	2.82 ± 0.06	2.77 ± 0.06	WW (AASW)
248	1.543	34.433	27.7832	13.4 ± 1.6	5.04 ± 0.08	4.98 ± 0.08	WW/DP-UCDW
327	1.811	34.548	27.8553	13.8 ± 1.6	6.64 ± 0.10	6.58 ± 0.10	DP-UCDW
416	1.874	34.627	27.9165	17.4 ± 1.3	8.68 ± 0.10	8.61 ± 0.10	DP-UCDW
416	1.874	34.627	27.9165	15.7 ± 1.3	7.94 ± 0.10	7.87 ± 0.10	DP-UCDW
742	1.702	34.704	28.012	21.5 ± 1.5	12.16 ± 0.14	12.06 ± 0.14	LCDW
1117	1.42	34.727	28.08	27.3 ± 1.3	15.28 ± 0.17	15.16 ± 0.17	LCDW
1678	0.755	34.704	28.171	28.6 ± 1.5	16.70 ± 0.19	16.58 ± 0.19	LCDW/AABW
2307	0.359	34.689	28.225	30.5 ± 1.4	18.11 ± 0.21	17.98 ± 0.21	AABW
2501	0.319	34.687	28.231	30.1 ± 1.3	16.82 ± 0.19	16.69 ± 0.19	AABW
Intercal: 52.98°S, 00.00°W, 2624 m bottom depth							
380	1.81	34.63	27.929	19.1 ± 1.2	9.93 ± 0.13	9.85 ± 0.13	UCDW
380	1.81	34.63	27.929	19.6 ± 1.4	9.90 ± 0.12	9.82 ± 0.12	UCDW
500	1.78	34.68	27.979	22.0 ± 1.2	12.14 ± 0.14	12.05 ± 0.14	LCDW
500	1.78	34.68	27.979	24.5 ± 1.5	13.44 ± 0.20	13.33 ± 0.20	LCDW
1000	1.22	34.71	28.094	27.4 ± 1.2	16.08 ± 0.20	15.96 ± 0.20	LCDW
1000	1.22	34.71	28.094	27.5 ± 1.3	16.11 ± 0.18	15.99 ± 0.18	LCDW
S5: 57.55°S, 00.03°W, 3932 m bottom depth							
134	-0.671	34.355	27.8713	19.7 ± 1.5	8.26 ± 0.11	8.17 ± 0.11	WW (AASW)
247	0.353	34.63	28.094	29.4 ± 1.5	15.64 ± 0.19	15.51 ± 0.19	WW (AASW)/ WDW
396	0.529	34.674	28.154	32.8 ± 1.4	19.10 ± 0.24	18.96 ± 0.24	WDW
692	0.422	34.685	28.202	36.1 ± 1.5	23.00 ± 0.24	22.84 ± 0.24	WDW
1185	0.154	34.677	28.2434	42.2 ± 1.5	26.59 ± 0.29	26.41 ± 0.29	WDW / WSDW
1776	-0.104	34.668	28.2872	49.4 ± 1.6	30.31 ± 0.32	30.10 ± 0.32	WDW / WSDW
2462	-0.346	34.66	28.332	60.6 ± 1.4	34.30 ± 0.36	34.04 ± 0.36	WSDW
3147	-0.502	34.655	28.3619	71.5 ± 1.6	34.42 ± 0.36	34.10 ± 0.36	WSDW
3848	-0.632	34.65	27.8713	83.1 ± 1.6	33.93 ± 0.37	33.57 ± 0.37	WSDW / WSBW
3848	-0.632	34.65	27.8713	82.5 ± 1.8	33.78 ± 0.38	33.42 ± 0.38	WSDW / WSBW

928 [1]: Uncertainties are $2\sigma_n$ (error on the mean). [2]: The excess $^{230}Th_{d\text{-}xs}$ is calculated using the
929 equation:

930 $$^{230}Th_{d-xs} = {}^{230}Th_{d-measured} - {}^{232}Th_{d-measured} \times \left(\frac{^{230}Th}{^{232}Th}\right)_{Lithogenic}$$, where the

931 $(^{230}Th/^{232}Th)_{Litogenic} = 4.0 \times 10^{-6}$ (mol/mol), close to average crust $^{230}Th/^{232}Th = 4.1 \times 10^{-6}$).
932 The lithogenic correction is small: generally less than 2% of $^{230}Th_d$ and occasionally reaching
933 6 to 11% in the surface waters of S2 and S1 respectively. Therefore the $^{230}Th_d$ and $^{230}Th_{d\text{-}xs}$
934 profiles do not differ significantly.
935
936
937
938

939 Table ES2: Particulate thorium data (in situ pump filtration)

Station	Depth (m)	Volume[1] (L)	$^{232}Th_p$ (pg/kg)[2]	$^{230}Th_p$ (pg/kg)[2]	$^{230}Th_{p\text{-}xs}$ (pg/kg)[2]	$^{230}Th_{p\text{-}xs}$ particulate fraction
S1						
	30	346	7.0 ± 0.1	0.076 ± 0.002	0.045 ± 0.003	4 %
	199	803	18.8 ± 0.3	0.209 ± 0.004	0.128 ± 0.004	6 %
	1242	997	32.3 ± 0.7	1.45 ± 0.03	1.31 ± 0.03	18 %
	2687	142	37.8 ± 0.5	1.309 ± 0.003	1.144 ± 0.004	8 %
	2732	1202	17.3 ± 0.5	1.8 ± 0.4	1.7 ± 0.4	12 %
	4628	610	371 ± 10	28.1 ± 0.4	26.5 ± 0.4	124 %
S2						
	20	315	4.1 ± 0.1	0.148 ± 0.004	0.130 ± 0.004	18 %
	257	814	8.9 ± 0.1	0.379 ± 0.003	0.340 ± 0.003	12 %
	601	961	5.4 ± 0.1	0.492 ± 0.004	0.469 ± 0.004	9 %
	1426	1053	9.1 ± 0.1	1.462 ± 0.009	1.422 ± 0.009	16 %
	1941	531	8.5 ± 0.1	0.752 ± 0.005	0.715 ± 0.005	5 %
	2859	515	8.9 ± 0.1	1.63 ± 0.01	1.59 ± 0.01	11 %
	3858	508	93.1 ± 1.2	8.51 ± 0.07	8.10 ± 0.07	48 %
S3						
	40	99	7.1 ± 0.1	0.163 ± 0.002	0.133 ± 0.002	12 %
	594	500	4.41 ± 0.04	0.686 ± 0.002	0.667 ± 0.002	13 %
	1058	967	5.1 ± 0.1	1.045 ± 0.003	1.023 ± 0.003	12 %
	1985	1128	5.5 ± 0.1	1.426 ± 0.004	1.402 ± 0.004	13 %
	3025	218	7.7 ± 0.1	1.778 ± 0.006	1.745 ± 0.006	12 %
	3024	552	8.0 ± 0.1	1.838 ± 0.005	1.804 ± 0.005	12 %
	4262	210	2.5 ± 0.0	0.344 ± 0.002	0.333 ± 0.002	4 %
S4						
	59	381	0.076 ± 0.001	0.0202 ± 0.0005	0.0198 ± 0.005	2 %
	169	702	1.48 ± 0.02	0.300 ± 0.001	0.294 ± 0.001	11 %
	258	903	2.42 ± 0.02	0.467 ± 0.001	0.457 ± 0.001	9 %
	743	984	2.23 ± 0.02	0.682 ± 0.002	0.672 ± 0.002	6 %
	1119	1069	2.82 ± 0.03	0.630 ± 0.002	0.617 ± 0.002	4 %
	1120	308	1.72 ± 0.02	0.368 ± 0.002	0.360 ± 0.002	2 %
	1682	1018	2.23 ± 0.02	0.727 ± 0.002	0.717 ± 0.002	4 %
	2273	938	6.07 ± 0.06	1.885 ± 0.005	1.858 ± 0.005	10 %
	2469	493	6.25 ± 0.06	1.850 ± 0.005	1.823 ± 0.005	11 %
S5						
	30	341	2.23 ± 0.01	0.706 ± 0.005	0.697 ± 0.005	
	139	872	2.1 ± 0.1	0.261 ± 0.002	0.251 ± 0.002	3 %
	248	927	2.5 ± 0.1	0.507 ± 0.003	0.496 ± 0.003	3 %
	694	127	3.6 ± 0.8	0.555 ± 0.009	0.539 ± 0.010	2 %
	1784	290	4.0 ± 0.4	0.714 ± 0.006	0.697 ± 0.006	2 %
	2478	1066	8.5 ± 0.1	1.726 ± 0.029	1.69 ± 0.03	5 %
	3172	905	11.6 ± 0.2	1.754 ± 0.006	1.703 ± 0.006	5 %
	3840	715	26.1 ± 0.3	2.966 ± 0.012	2.852 ± 0.012	8 %

940 [1] Fraction of the volume of filtered water used for Thorium analysis. [2] Uncertainties are $2\sigma_n$
941 (error on the mean).
942

943

Table ES3: Total thorium isotopes recalculated on neutral density surfaces

	Depth (m)	θ (°C)	Salinity	^{232}Th (pg/kg)	error	^{230}Th (fg/kg)	error
γ^n = 27.865 kg/m^3							
S1	-1550	2.732	34.695	10.67	0.15	72.4	1.5
S2	-1631	2.564	34.667	11.51	0.12	36.3	1.3
S3	-1227	2.44	34.644	10.07	0.13	25.1	2.9
S4	-345	1.838	34.563	7.59	0.11	16.8	1.8
S5	-98	-0.665	34.348	8.52	0.11	21.8	0.1
γ^n = 28.094 kg/m^3							
S1	3073	1.86	34.827	15.1	0.2	60.7	1.5
S2	3082	1.849	34.823	17.3	0.8	52.9	0.2
S3	2440	1.722	34.756	15.2	0.2	32.1	1.3
S4	1205	1.322	34.726	15.9	0.2	29.3	1.3
intercal	-999.6	1.205	34.71	16.7	0.2	30.1	1.2
intercal	-999.6	1.205	34.71	16.7	0.2	30.2	1.3
S5	247	0.28616	34.619	16.1	0.2	31.9	1.6

Fig. ES1: comparison of particulate ^{232}Th collected by in situ pump and Niskin filtrations.

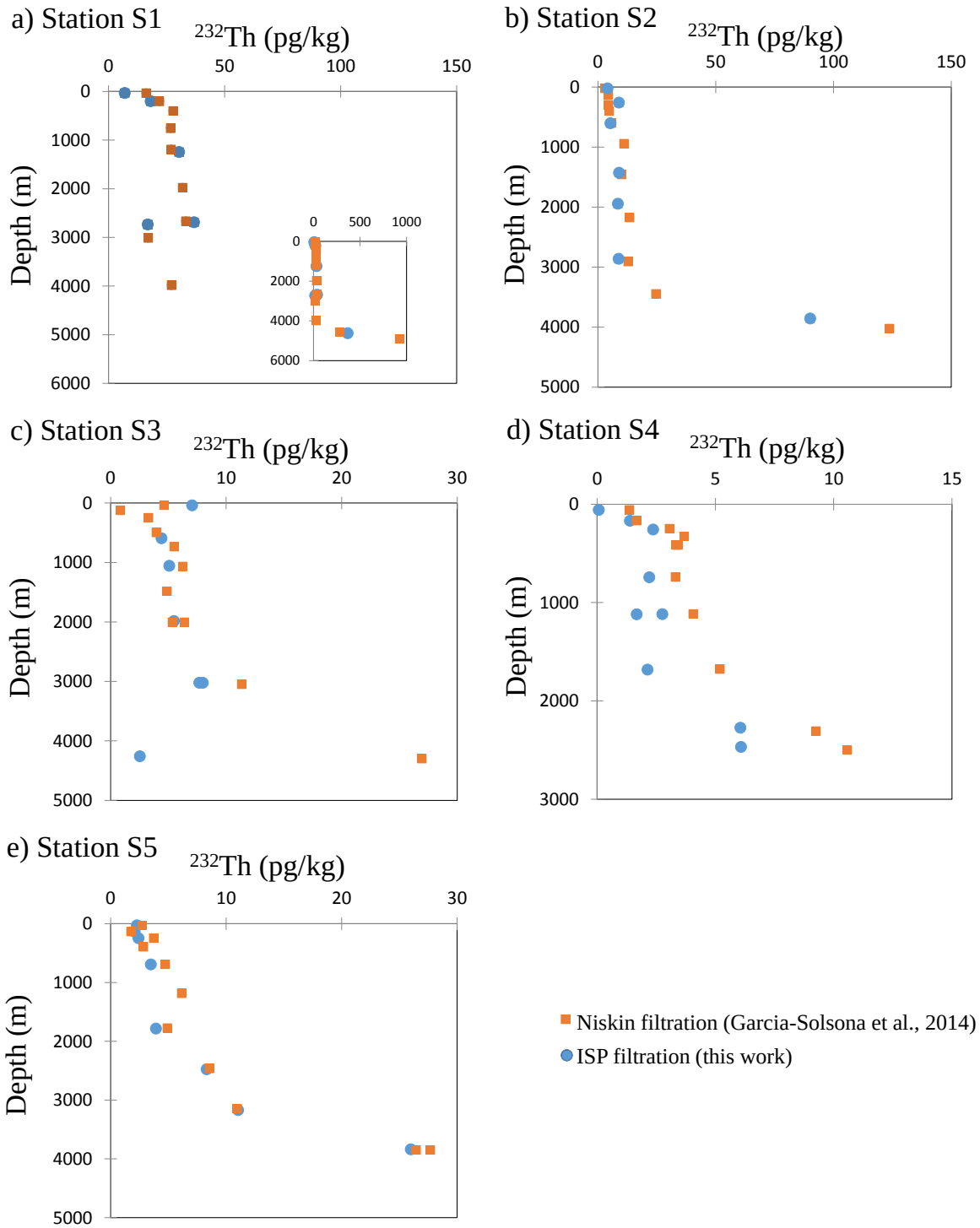

950

Figure ES2: Dissolved Th isotopes BGH sections. (a) $^{232}Th_d$. (b): $^{230}Th_d$. White curves: neutral density surfaces.

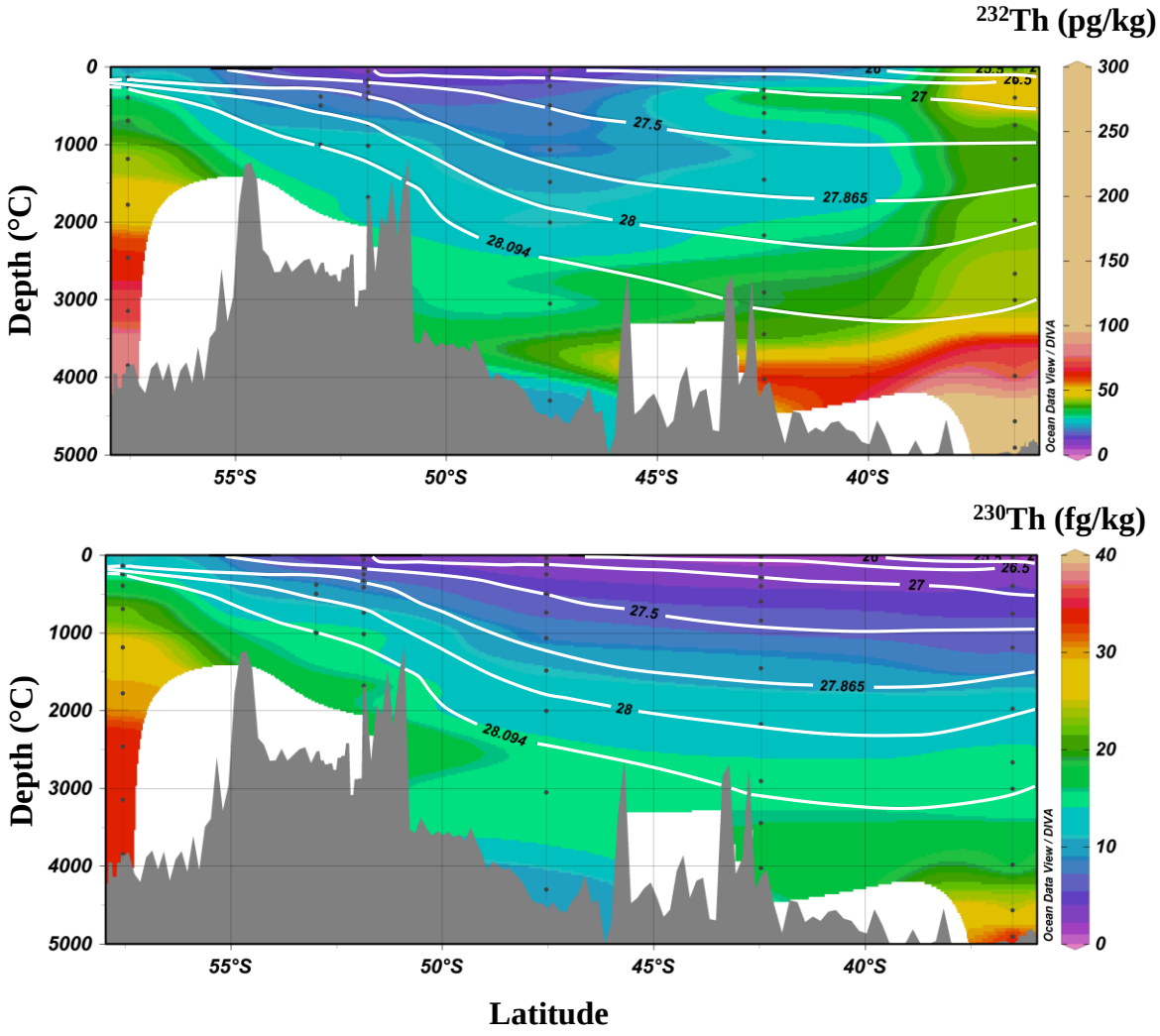

Figure ES3: Dissolved Th comparison between 2 stations of the BGH and Zero-Drake sections. $^{232}Th_d$ and $^{230}Th_d$ are plotted versus potential density anomaly in order to reduce hydrographical variations between the 2 cruises.

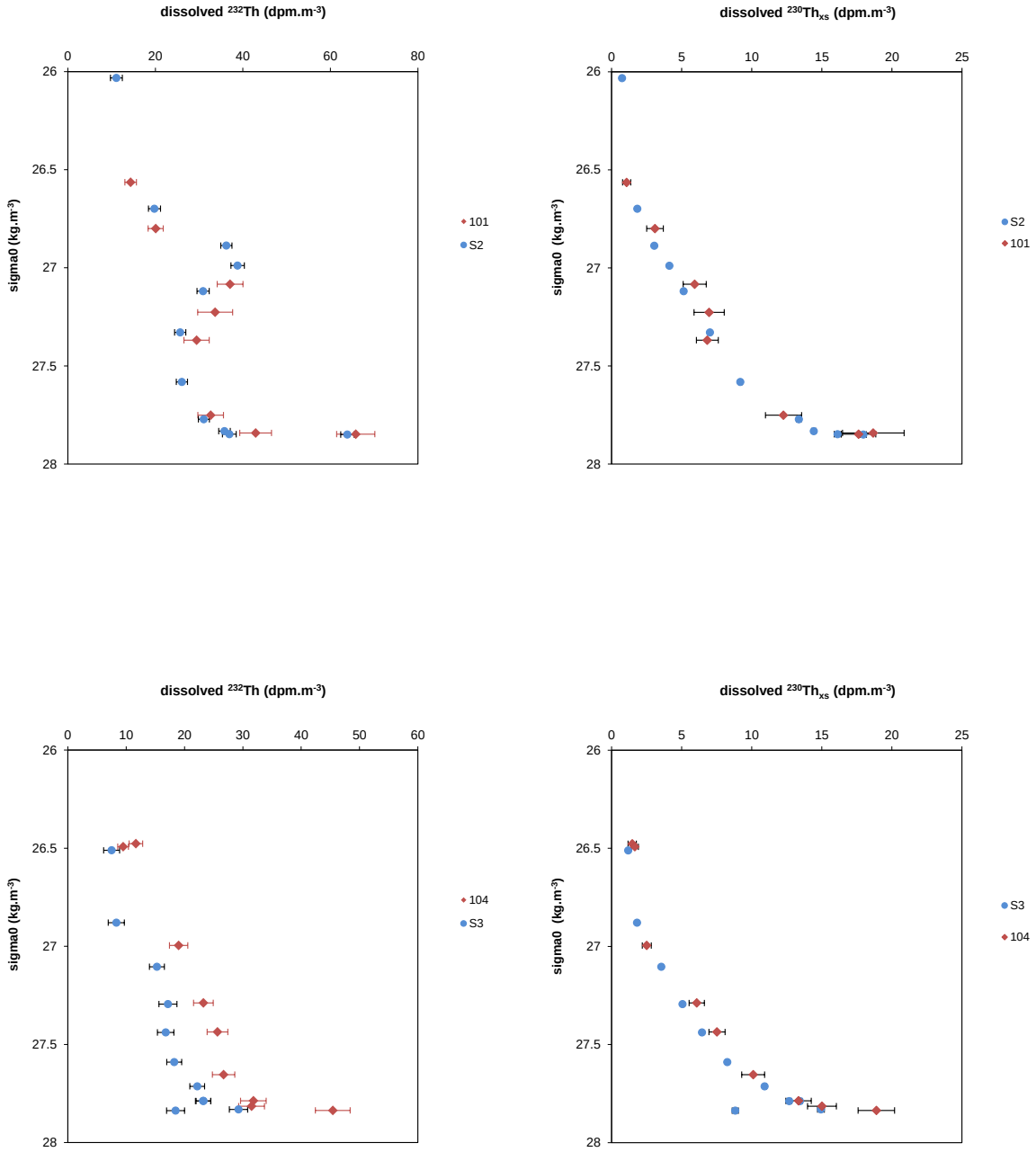

976